Period spacings of *γ* Doradus pulsators in the *Kepler* field: Rossby and gravity modes in 82 stars

Gang Li,[1,2]★ Timothy Van Reeth,[1,2] Timothy R. Bedding [ID],[1,2]★ Simon J. Murphy[1,2] and Victoria Antoci[2]

[1]*Sydney Institute for Astronomy (SIfA), School of Physics, University of Sydney, Camperdown NSW 2006, Australia*
[2]*Stellar Astrophysics Centre, Department of Physics and Astronomy, Aarhus University, Ny Munkegade 120, DK-8000 Aarhus C, Denmark*

ABSTRACT

Rossby modes are the oscillations in a rotating fluid, whose restoring force is the Coriolis force. They provide an additional diagnostic to understand the rotation of stars, which complicates asteroseismic modelling. We report 82 *γ* Doradus stars for which clear period spacing patterns of both gravity and Rossby modes have been detected. The period spacings of both show a quasi-linear relation with the pulsation period, but the slope is negative for the gravity modes and positive for the Rossby modes. Most Rossby modes have $k = -2$, $m = -1$. For only one star, a series of $k = -1$, $m = -1$ modes is seen. For each pattern, the mean pulsation period, the mean period spacing, and the slope are measured. We find that the slope correlates with the mean period for Rossby mode patterns. The traditional approximation of rotation is used to measure the near-core rotation rate, assuming the star rotates rigidly. We report the near-core rotation rates, the asymptotic period spacings, and the radial orders of excited modes of these 82 main-sequence stars. The near-core rotation rates lie between 0.6 and $2.3\,\mathrm{d^{-1}}$. Six stars show surface rotation modulations, among which only KIC 3341457 shows differential rotation, whilst the other five stars have uniform rotations. The radial orders of excited modes show different distributions for the dipole and quadrupole gravity modes versus the Rossby modes.

Key words: stars: oscillations – stars: rotation – stars: variables.

1 INTRODUCTION

Rotation is one of the key parameters that decides how stars evolve, since it affects many physical processes of the stellar interior (e.g. Maeder 2009; Mathis et al. 2013). For example, differential rotation induces an extra shear mixing and changes the local abundances of chemical elements. It can transport fuel into the nuclear burning regions and extend the lifetime of the star (e.g. Prat et al. 2018; Van Reeth et al. 2018). Differential rotation, both in radial and latitudinal directions, has been seen in the Sun and some sun-like stars (e.g. Thompson et al. 1996; Couvidat et al. 2003; Benomar et al. 2018), and A-type main-sequence stars (e.g. Hatta et al. 2019). However, our understanding of rotation is still incomplete (e.g. Aerts et al. 2014; Cazorla et al. 2017).

In the rotating frame, the Coriolis force is defined to maintain Newton's laws of motion. This kind of inertial force acts as the restoring force for Rossby modes (r modes, Papaloizou & Pringle

1978). Rossby modes are inertial modes, unlike the well-known gravity modes and pressure modes from asteroseismology, whose restoring forces are buoyancy and the pressure gradient, respectively. Rossby modes involve global toroidal motions coupling with the spheroidal motion by the Coriolis force, whose compression and expansion lead to the temperature perturbations and hence make the Rossby modes visible (Pedlosky 1982; Saio et al. 2018a). This wave propagates in the direction retrograde to the rotation and is confined to the mid-latitudes (Saio 1982; Lee & Saio 1997), introducing the possibility of measuring the stellar inclination in future (Saio et al. 2018a). Rossby waves also have discrete frequencies that are smaller than the rotation frequency in the inertial frame (Provost, Berthomieu & Rocca 1981). We refer the interested reader to Saio et al. (2018a), and the references therein, for a more extensive theoretical discussion about r modes.

Rossby waves are seen or predicted in many types of rotating systems. They appear in planetary atmospheres (Rossby 1939) and play a key role in accurate weather forecasting (e.g. Screen & Simmonds 2014). The Sun rotates slowly but the Rossby waves still can be observed by tracking the coronal brightpoints and the south-north helioseismic travel times (McIntosh et al. 2017; Löptien

et al. 2018; Liang et al. 2018). They have the potential to improve our understanding of energy transfer, solar activity, and space weather (Zaqarashvili et al. 2015). Many questions remain. For example, how do the Rossby waves affect the protoplanetary disc (Lovelace & Romanova 2014) and how do they affect the evolution of DA white dwarfs and neutron stars (Saio 1982; Berthomieu & Provost 1983; Andersson 1998; Brown & Ushomirsky 2000)?

In this paper, we conduct an observational study of γ Doradus stars with resolved gravity and Rossby modes. The brightness variations of γ Dor stars have been observed for several decades (e.g. Cousins & Warren 1963; Balona, Krisciunas & Cousins 1994). They are F- to A-type main-sequence stars with typical masses between $1.4\,\mathrm{M_\odot}$ and $2.0\,\mathrm{M_\odot}$, burning hydrogen in their convective cores (Van Reeth et al. 2015b). The pulsations in γ Dor stars are mainly high radial order ($20 \lesssim n \lesssim 120$) low degree ($l \leq 4$) gravity modes (e.g. Balona et al. 1994; Kaye et al. 1999; Van Reeth, Tkachenko & Aerts 2016; Saio et al. 2018b), which are useful for investigating the interior of stars since they have the highest mode energy in the near-core regions (Triana et al. 2015; Van Reeth et al. 2016). Shibahashi (1979) pointed out that the periods of high radial order g modes ($n \gg l$) are equally spaced for chemically homogeneous non-rotating stars. Miglio et al. (2008) considered the effect of chemical composition gradients and found that dips or glitches appear in the period spacing patterns. Rotation also affects period spacings, causing the spacing of the prograde ($m > 0$) and zonal ($m = 0$) modes to decrease linearly with increasing period, and overall spacing to increase for the retrograde ($m < 0$) modes in the inertial reference frame (Bouabid et al. 2013; Ouazzani et al. 2017).

The long pulsation periods (~1 d), small period spacings (~1000 s), and the low pulsation amplitudes (~0.1 per cent variation) are challenging for ground-based observations. Thanks to the high precision and the long time-base of *Kepler* data (Borucki et al. 2010; Koch et al. 2010), period spacing patterns of tens of γ Dor stars have been detected. Some of these stars rotate slowly, hence nearly regular period spacings and rotation splittings are seen (e.g. Kurtz et al. 2014; Keen et al. 2015; Saio et al. 2015; Murphy et al. 2016; Li et al. 2019). However, most γ Dor stars rotate rapidly and the period spacings change significantly with period (e.g. Bedding et al. 2015; Van Reeth et al. 2015a; Saio et al. 2018b; Christophe et al. 2018). Besides g modes, r modes were also found in γ Dor stars by Van Reeth et al. (2016) and Saio et al. (2018a). The resolved r modes generally show a quasi-linearly increasing period spacing with increasing period. However, the period spacing in r modes drops at the larger period region (see the observation and theory in Saio et al. 2018a). Saio et al. (2018a) also explained observed power excesses in the periodogram as unresolved Rossby modes, in which the discrete frequencies are below the frequency resolution.

Here, we report 82 γ Dor stars in which the period spacing patterns of g and r modes are both seen. The co-existence of prograde and retrograde modes spacings breaks the correlation between the asymptotic spacing and the near-core rotation rate, and allows us to determine their values more precisely (Van Reeth et al. 2016). The resolved r- and g-mode spacings also give many new possibilities for future research. They can be used in detailed asteroseismic modelling analyses (e.g. Aerts et al. 2018b) to study the inner physics of main-sequence stars, such as differential rotation and angular momentum transport (Aerts, Mathis & Rogers 2018a; Van Reeth et al. 2018).

In Section 2, we briefly review the light-curve reduction and pattern identification introduced by Li et al. (2019). In Section 3, we show how the traditional approximation of rotation (TAR) is used to model the observed patterns and reveals the near-core rotation rate. In Section 4, we report the observational results, such as the HR diagrams of our stars using *Gaia* data, the slope-period relations of g and r modes, near-core and surface rotation rates, and radial order distributions. Finally, we summarize our findings in Section 5.

2 PATTERN EXTRACTION

We used 4-yr *Kepler* long-cadence (LC; 29.45-min sampling) light curves from the multiscale MAP data pipeline (Stumpe et al. 2014). In each quarter, the light curve was divided by a second-order polynomial fit to remove any slow trend. We computed the Fourier transform and extracted the frequencies until the signal-to-noise ratio (S/N) was smaller than 3. The frequency uncertainty is given by

$$\sigma(f) = 0.44 \frac{\langle a \rangle}{a} \frac{1}{T}, \tag{1}$$

where $\langle a \rangle$ is the noise level in the amplitude spectrum, a is the amplitude of peak, and T is the total time span of the *Kepler* data ($T \simeq 1470\,\mathrm{d}$) (Montgomery & Odonoghue 1999; Kjeldsen 2003). Considering the S/N threshold, the frequency uncertainty in our work is smaller than $1 \times 10^{-4}\,\mathrm{c/d}$.

Combination frequencies are seen in some γ Dor stars. They form several frequency groups in the power spectrum but the understanding of them is still an open question (Kurtz et al. 2015; Saio et al. 2018b). Likely combination frequencies were determined by the condition

$$|n_i f_i + n_j f_j - f_k| < 0.0002\,\mathrm{c/d}, \tag{2}$$

where f_i and f_j are parent frequencies, n_i and n_j are the coefficients, and f_k is the combination candidate. We selected the 20 highest peaks as parent frequencies and set $|n_i| + |n_j| \leq 2$. In our work, the patterns dominated by the combination frequencies could be explained as the higher degree prograde sectoral oscillations following Saio et al. (2018b).

A cross-correlation algorithm was implemented to detect the period spacing patterns between 0.2 and 2 d (Li et al. 2019). We built a template to imitate the shape of periodogram, which was specified by the central peak's period P_c, the central peak's period spacing ΔP_c, the slope $\Sigma \equiv \mathrm{d}\Delta P / \mathrm{d}P$, and the number of peaks. The product of the template and the observed periodogram was used to measure the goodness of fit. The larger the product, the better the template described the observed pattern.

Then, the pattern is fitted by the formula

$$P_i = \Delta P_0 \frac{(1 + \Sigma)^i - 1}{\Sigma} + P_0 = \Delta P_0 (n' + \epsilon) \tag{3}$$

with the assumption that the period spacing changes linearly with period. Here, P_i is the ith peak, P_0 is the first peak, ΔP_0 is the first period spacing, Σ is the slope in the linear assumption, $n' \equiv \frac{(1+\Sigma)^i - 1}{\Sigma}$ is the normalized index, and ϵ is the ratio $P_0 / \Delta P_0$ (Li et al. 2019). Due to the occasional missing peaks, not all the period spacings can be calculated. This formula can be used to include isolated peaks, where there is no adjacent peak to calculate the period spacing value, and is helpful in calculating the radial order differences. Equation (3) also allows us to make an échelle diagram for less clear period spacing patterns and guide the pattern identification.

We can assign an angular degree l and an azimuthal order m to gravity modes. For the Rossby modes, the angular degree l is not defined and the value k is used instead (Lee & Saio 1997). For gravity modes, $k = l - |m|$. This paper adopts the convention

that positive m represents the prograde modes, whilst negative m represents retrograde modes.

2.1 An example: KIC 3240967

We present the period spacing patterns of KIC 3240967 as an example in Fig. 1. KIC 3240967 is the main-sequence γ Dor star with effective temperature of 7054 ± 80 K (Mathur et al. 2017). Its near-core rotation rate is $1.2857 \pm 0.0008 \, \mathrm{d}^{-1}$ determined by the g and r modes pulsations (see section 3.2). Panel (a) of Fig. 1 shows the periodogram from 0.2 to 2.4 d, where the vertical dashed lines show the best fit from equation (3) for each pattern. We found two period spacing patterns around 0.55 and 0.95 d. The left pattern, marked by the blue dashed lines, comprises the dipole sectoral ($m = l = 1$) g modes, whilst the right one, marked by the black dashed lines, comprises the even ($k = -2$) retrograde ($m = -1$) r modes (for the geometry of r modes, please refer to the fig. 2 in Saio et al. 2018a). The mode identifications are made based on the TAR fit in Section 3.2 and previous literature Van Reeth et al. (2018) and Saio et al. (2018a). Apart from these two patterns, the periodogram also displays two groups dominated by combination frequencies, located around 0.3 and 1.5 d. The first is at twice the g-mode frequencies and the second is at the difference between the g- and r-mode frequencies.

Panel (b) in Fig. 1 depicts the period spacing versus period. The period spacing for g modes decreases from 500 to 200 s with increasing period. For the r-mode pattern, the period spacing increases from 200 to 1000 s with increasing period. Both patterns show deviations from the linear model, such as the dip at 0.92 d in the r-mode pattern, which is likely to be caused by the chemical composition gradient near the outer edge of the convective core (Miglio et al. 2008). The period spacing in the r-mode pattern also shows a drop at the longest period spacings [see the right side of Fig. 1(h) for example], caused by the rapid change of the eigenvalue λ in the Laplace tidal equation (see Section 3 for example).

Panels (c) and (d) zoom in on the g modes from panels (a) and (b), whilst panels (g) and (h) do the same for the r modes. In Panels (e) and (i), the échelle diagrams are plotted sideways. The x-axis is the pulsation period, whilst the y-axis is the term $P^{\mathrm{obs}} - n^{'} \Delta P$ from the fit of equation (3). For the peaks that do not belong to the pattern, we plotted them at the location that minimized the value $P^{\mathrm{obs}} - n^{'} \Delta P$. Therefore, the y-axis reflects the deviations from the linear fit, similar to the curvature in the échelle diagram of solar-like oscillators (e.g. Mazumdar et al. 2014). Panels (f) and (j) show the normalized sideways échelle diagram. The x-axis is the index of peaks, counting the first peak as 0, and the y-axis is the deviation over the local period spacing $(P^{\mathrm{obs}} - n^{'} \Delta P)/\Delta P$ expressed as a percentage.

3 NEAR CORE ROTATION

3.1 TAR fitting algorithm

We used the TAR to fit the period spacing patterns and derive the near-core rotation rate (Eckart 1960; Lee & Saio 1987; Townsend 2005). In the TAR, the θ-component of the rotation vector and the effects of the centrifugal force are ignored (Lee & Saio 1997). The TAR saves computational time and it provides a reliable approximation of the influence of rotation on the pulsation periods. Many stars have been investigated using the TAR to determine the near-core rotation rates (e.g. Van Reeth et al. 2016; Guo, Gies & Matson 2017; Saio et al. 2018a,b) and we followed the method

reported by Van Reeth et al. (2016). We also assumed that all the stars rotate rigidly, consistent with recent observations (e.g. Kurtz et al. 2014; Saio et al. 2015; Murphy et al. 2016; Schmid & Aerts 2016; Guo et al. 2017; Aerts et al. 2018a; Van Reeth et al. 2018).

The spin parameter is defined as

$$s \equiv \frac{2 f_{\mathrm{rot}}}{f_{\mathrm{co}}}, \tag{4}$$

where f_{rot} is the rotation frequency and f_{co} is the pulsation frequency in the co-rotating frame. The spin parameter s represents the validity of the TAR. Ballot et al. (2012) showed that the TAR remains valid for the pulsation frequencies of gravito-inertial modes with $s < 1$, even in the case of large stellar rotation rates. This was further studied by Ouazzani et al. (2017). The authors found that the TAR is well suited for the analysis of prograde and zonal modes when the stellar rotation is less than 50 per cent of the critical rotation rate, whilst retrograde gravito-inertial modes can be analysed with the TAR for rotation rates up to 25 per cent of the critical rotation rate. However, the TAR has also been used to determine the near-core rotation rate in moderate- to fast-rotating stars, by fitting observed r modes and prograde gravito-inertial modes, with satisfactory results (e.g. Saio et al. 2018b; Van Reeth et al. 2018).

The pulsation period in the co-rotating frame, given by the TAR, is

$$P^{\mathrm{TAR}}_{nlm,\mathrm{co}} = \frac{\Pi_0}{\sqrt{\lambda_{l,m,s}}} \left(n + \varepsilon_g \right), \tag{5}$$

where Π_0 is the asymptotic period spacing, n is the radial order, the phase term ε_g is set as 0.5, and $\lambda_{l,m,s}$ is the eigenvalue of the Laplace tidal equation, which is specified by the angular degree l or the value k, the azimuthal order m and the spin parameter s.

Equation (5) becomes the asymptotic relation (Shibahashi 1979) when $s \to 0$:

$$P_{nl} = \frac{\Pi_0}{\sqrt{l \left(l + 1 \right)}} \left(n + \varepsilon_g \right). \tag{6}$$

The period in the inertial frame is obtained by

$$P^{\mathrm{TAR}}_{\mathrm{in}} = \frac{1}{1/P^{\mathrm{TAR}}_{\mathrm{co}} + m \cdot f_{\mathrm{rot}}}. \tag{7}$$

The period spacing is calculated with equations (5) and (7) to be

$$\Delta P^{\mathrm{TAR}}_{j,\mathrm{in}} = P^{\mathrm{TAR}}_{j+1,\mathrm{in}} - P^{\mathrm{TAR}}_{j,\mathrm{in}}, \tag{8}$$

where j is the index sorted by the ascending period values. Note that the index j is not the radial order since the radial order for r modes drops with increasing period in the inertial reference frame.

The TAR fit can only give the slope, rather than the exact locations of peaks. Hence, we interpolated the period spacing $\Delta P^{\mathrm{interp}}_i$ at the observational period P^{obs}_i using ΔP^{TAR} and P^{TAR}. We defined the log likelihood function $\ln L$ as

$$\ln L \left(\Delta P | P^{\mathrm{obs}}, \Pi_0, f_{\mathrm{rot}}, k, m \right)$$
$$= -\frac{1}{2} \sum_j \left[\frac{\Delta P^{\mathrm{obs}}_j - \Delta P^{\mathrm{interp}}_j}{\sigma^2_j} + \ln \left(2\pi \sigma^2_j \right) \right], \tag{9}$$

where σ is the residual of the best-fitting result. Since the observed patterns showed glitches and dips caused by the chemical composition gradient that the TAR does not take into account, and these variations are larger than the formal error margins on the pulsation periods, we used the residuals rather than the period spacing uncertainties to estimate the TAR model uncertainty. The data points below -1σ of the linear fit were excluded, because they were likely to be dips and mislead the fitting. We ran a Markov
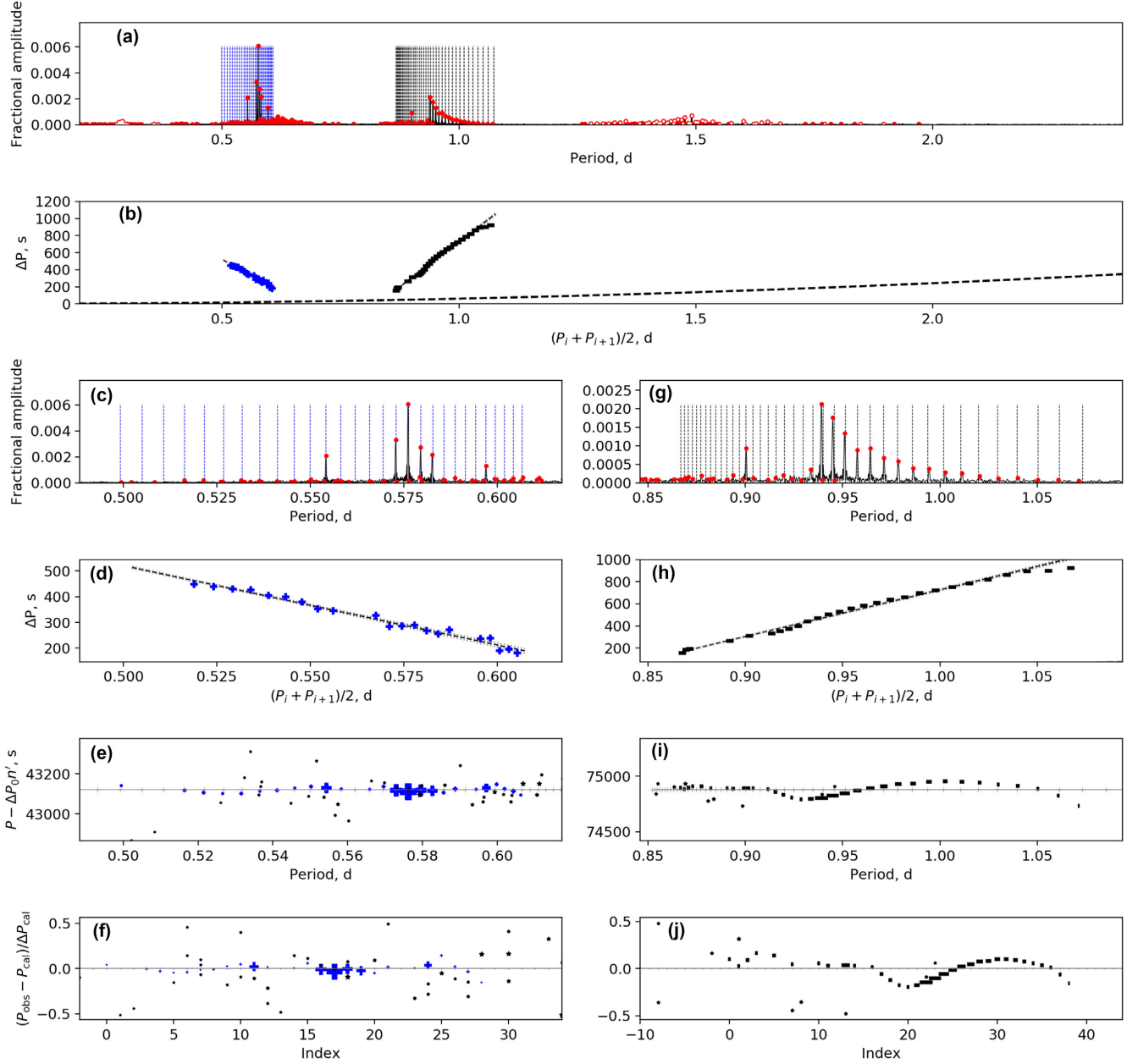
Figure 1. The g- and r-mode patterns of KIC 3240967. (a) The amplitude spectrum with *x*-axis of period. The solid red circles present the detected independent frequencies, whilst the open red circles show the combination frequencies. The vertical dashed lines are the linear fits for each pattern. The *x*-axis range is set from 0.2 to 2.4 d for consistency for all stars. We found two independent frequency groups around 0.55 and 0.95 d and two combination frequency groups around 0.3 and 1.5 d. There are two period spacing patterns. The blue one on the left is the $l = 1$, $m = 1$ g modes, whilst the black one on the right is the $k = -2$, $m = -1$ r modes. (b) The period spacing patterns of KIC 3240967. The linear fits and uncertainties are shown by the black and grey dashed lines. The blue plus symbols are the g modes and the black minus symbols are the r modes. (c) and (d) The detail of the spectrum and period spacing pattern of g modes. (e) The sideways échelle diagram of the g pattern. The black stars are the messy peaks. (f) The normalized sideways échelle diagram of the g-modes pattern. (g)−(j) Same as (c–f) but for the r-mode patterns.

Chain Monto Carlo (MCMC) code to maximize the likelihood function equation (9) using the EMCEE package (Foreman-Mackey et al. 2013). The eigenvalue λ was given by GYRE (Townsend & Teitler 2013). The fit has two variables because the value *k* and the azimuthal order *m* were given based on the mode identification, so only the asymptotic spacing Π_0 and the near-core rotation rate f_{rot} were free parameters. The initial value of Π_0 was 4200 s, which is the most likely value of γ Dor stars from Van Reeth et al. (2016). The initial guess of f_{rot} was chosen to be halfway between the prograde

g and retrograde r patterns because the period of the prograde mode in the inertial frame is smaller than the rotation period, and vice versa for the r modes. The range of Π_0 was from 2000 to 20 000 s to cover the typical range of both γ Dor and Slowly Pulsating B (SPB) stars. We searched for the best-fitting solution with a rotation rate f_{rot} between 0 and 5 d^{-1}. The upper limit of f_{rot} exceeds the critical rotation rate at which the centrifugal force causes a star to break apart. However, it is only selected to make sure that we can find a proper solution for every star. Based on our results (Fig. 11 shown
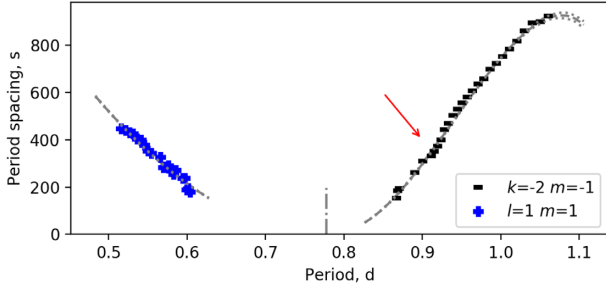
Figure 2. The TAR fit of KIC 3240967. The blue plus symbols show the $l = 1$, $m = 1$ gravity modes and the black minus symbols show the $k = -2$, $m = -1$ Rossby modes. The dashed grey curves display the best-fitting result. The error margins are plotted by the dotted lines, which are only visible at the right edge of the plot. The vertical dashed line denotes the fitted rotation period. The red arrow shows a dip.
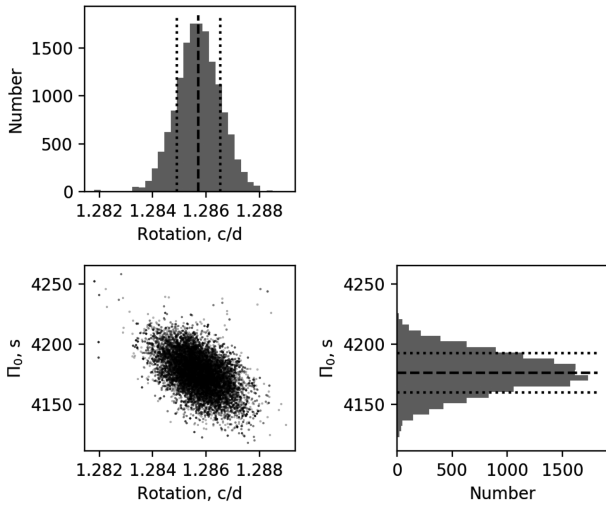
Figure 3. The posterior distributions for the TAR fit to KIC 3240967 using equation (9). The dashed lines are the medians and the dotted lines show the $\pm 1\sigma$ areas.

in Section 4.6), there is no star that reaches this limit. We also set the radial orders from 5 to 150.

3.2 TAR fitting of KIC 3240967

We again use KIC 3240967 to show how the TAR performed. Fig. 2 gives the TAR fit result. The dashed curves that pass through the data points represent the best model, whilst the dotted lines are the $\pm 1\sigma$ region. We found that the model can explain the observational patterns. The observed period spacings of r-modes follow the TAR prediction and the slope changes very little with period except for a drop near the end of the r pattern, which is caused by the rapid change of the eigenvalue λ (see the fig. 1 of both Townsend 2003; Saio et al. 2018a). The theoretical slope of the g-mode period spacing pattern also changes with the period but only slightly. A dip in r-modes appears at $P \sim 0.91$ d (see the red arrow in Fig. 2), which might be the deviation from the asymptotic expression with the TAR, or is evidence of a chemical composition gradient effect (Miglio et al. 2008).

Fig. 3 gives the posterior distributions of KIC 3240967. The best-fitting rotation rate is $f_{\rm rot} = 1.2857 \pm 0.0008\,{\rm d}^{-1}$ and the asymptotic spacing is $\Pi_0 = 4180 \pm 20$ s. Because the prograde and
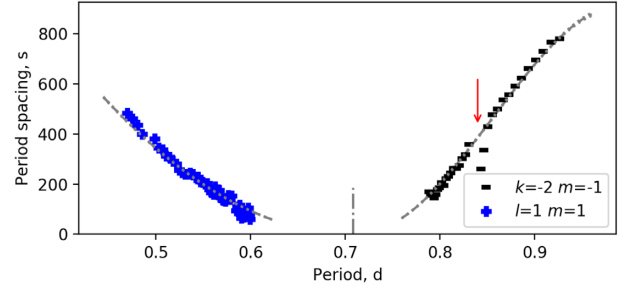
Figure 4. Same as Fig. 2 but for KIC 11775251. An obvious dip are seen in r-modes pattern at 0.85 d. Since the dip has been excluded, the fitting curves pass through other data points and do not be affected. The red arrow shows a dip.

retrograde modes co-exist, the correlation between $f_{\rm rot}$ and Π_0 is weak, so we have a better constraint on the near-core rotation.

Large dips are seen in some stars, for example, KIC 11775251, and were omitted from the TAR fit. Fig. 4 shows the period spacing patterns and the TAR fit of KIC 11775251, in which a dip of r modes is seen around ~ 0.85 d denoted by the red arrow. Since the dip has been removed, the fitting curves pass through other data points and are not affected. The fitting results are $\Pi_0 = 4040 \pm 20$ s and $f_{\rm rot} = 1.4115 \pm 0.0007\,{\rm d}^{-1}$.

4 PERIOD SPACING PATTERNS OF 82 γ DOR STARS

We inspected the Fourier transforms of stellar light curves for 1593 *Kepler* targets with effective temperatures from 6600 to 10 000 K. Among these, we found 82 stars that show resolved period spacing patterns of both g and r modes. Table 1 shows mode identifications, observational pattern parameters, asymptotic spacings, near-core rotation rates, and the radial order ranges for our sample. The means of the periods are the average of all detected peaks. The mean period spacing is the slope of the linear fit between P_i and the index i, which is similar to the method used by White et al. (2011) to find p-mode frequency spacings ($\Delta\nu$) for solar-like oscillators. In Appendix A, we show the equivalent of Figs 1–3 for all 82 stars with g and r modes, sorted by rotation rate. The axes of panels (a) and (b) are the same for all figures, to make the comparison straightforward. Example diagrams are shown in Figs A1–A3. The figures for the other 81 stars are available as supplementary online material. Every star shows both downward and upward period spacing patterns, which are $l = 1$, $m = 1$ g modes and $k = -2$, $m = -1$ r modes, respectively. As the rotation decreases, both the g- and r-mode patterns move from left to right and the period gap between them increases. We also found 17 patterns which are identified as the $l = 2$, $m = 2$ g modes (listed in Table 1). Only one star (KIC 5721632) has $k = -1$, $m = -1$ r modes.

4.1 Stars on the HR diagram

Fig. 5 shows the HR diagram of the 78 γ Dor stars (red circles) with clear r-mode patterns. Four stars are excluded since their data quality are insufficient (Their KIC numbers are: 2575161, 4077558, 5706866, and 9594007). Our exclusion conditions are (1) the fractional parallax uncertainty is larger than 20 per cent; (2) the star is 0.4 dex below the zero-age main-sequence (ZAMS); (3) there is no parallax or parallax error in *Gaia* DR2; and (4) the star is identified as a binary. We took the effective temperatures $T_{\rm eff}$ from the latest

Table 1. The mode identifications, mean pulsation periods ⟨P⟩, mean period spacings ⟨ΔP⟩, slopes, asymptotic spacings, near-core rotation rates, the ranges of radial orders *n,* and ranges of spin parameters *s* of 82 stars in this paper.

KIC	k	m	⟨P⟩ d	⟨ΔP⟩ s	mean Σ d/d	Π_0 s	f_{rot} d^{-1}	n min	n max	s min	s max
2575161	0	1	0.4	250	-0.0466 ± 0.0009	4470 ± 20	1.833 ± 0.001	20	54	3.6	10.0
	−2	−1	0.7	580	0.0753 ± 0.0004			8	27	7.3	16.2
2710594	0	1	0.7	360	-0.0290 ± 0.0003	4000 ± 10	0.9920 ± 0.0006	27	86	2.3	7.9
	−2	−1	1.2	470	0.0381 ± 0.0005			20	64	7.4	18.0
3240967	0	1	0.6	320	-0.0344 ± 0.0002	4180 ± 20	1.2857 ± 0.0008	30	58	3.5	7.0
	−2	−1	0.9	450	0.0507 ± 0.0004			13	51	7.2	19.4
3341457	0	1	0.4	120	-0.0292 ± 0.0007	3840 ± 40	1.859 ± 0.001	41	79	6.5	12.7
	−2	−1	0.6	100	0.0526 ± 0.0009			34	60	17.2	30.2
3445468	0	1	0.6	200	-0.0266 ± 0.0003	3860 ± 10	1.2037 ± 0.0007	35	101	3.5	10.9
	−2	−1	1.0	560	0.0377 ± 0.0006			16	42	7.4	14.3
3448365	0	1	0.7	330	-0.0301 ± 0.0008	4190 ± 10	1.0736 ± 0.0005	28	80	2.7	8.0
	−2	−1	1.1	380	0.0440 ± 0.0003			17	69	7.6	21.9
3449625	0	2	0.3	300	-0.0317 ± 0.0008	3970 ± 10	1.0514 ± 0.0005	24	47	1.0	2.2
	0	1	0.7	380	-0.0304 ± 0.0002			27	75	2.4	7.1
	−2	−1	1.1	310	0.0491 ± 0.0009			28	65	9.6	19.2
3626325	0	1	0.9	440	-0.0248 ± 0.0005	3910 ± 10	0.7820 ± 0.0005	45	81	2.9	5.8
	−2	−1	1.6	690	0.0203 ± 0.0006			22	53	7.0	12.0
3868382	0	2	0.4	360	-0.0325 ± 0.0002	4450 ± 10	0.8441 ± 0.0004	14	65	0.5	2.7
	0	1	0.7	630	-0.0320 ± 0.0003			20	68	1.5	5.7
	−2	−1	1.5	530	0.0358 ± 0.0002			18	62	7.3	16.8
3942392	0	2	0.2	120	-0.0402 ± 0.0005	4270 ± 30	1.627 ± 0.001	24	62	1.8	4.8
	0	1	0.5	230	-0.0383 ± 0.0003			26	63	3.9	9.8
	−2	−1	0.7	120	0.0511 ± 0.0004			33	62	16.5	30.5
3971170	0	1	0.7	190	-0.0264 ± 0.0007	3920 ± 30	1.198 ± 0.001	46	90	4.7	9.8
	−2	−1	1.0	240	0.066 ± 0.001			37	57	12.8	18.9
4069477	0	1	0.5	170	-0.0328 ± 0.0004	4020 ± 30	1.531 ± 0.002	39	73	5.3	10.3
	−2	−1	0.8	640	0.0532 ± 0.0006			12	25	7.6	11.7
4076350	0	2	0.3	160	-0.0583 ± 0.0008	3470 ± 20	1.248 ± 0.001	38	56	1.8	2.6
	0	1	0.6	230	-0.0454 ± 0.0009			46	77	4.3	7.7
	−2	−1	1.0	430	0.0412 ± 0.0007			19	53	7.6	16.5
4077558	0	1	0.6	260	-0.0340 ± 0.0001	3960 ± 10	1.2063 ± 0.0008	29	86	3.0	9.4
	−2	−1	1.1	620	0.0409 ± 0.0007			12	39	7.0	13.7
4261149	0	1	0.7	220	-0.0209 ± 0.0009	4820 ± 40	1.1251 ± 0.0009	44	82	5.3	10.4
	−2	−1	1.1	440	0.024 ± 0.005			26	37	11.0	14.6
4448157	0	1	0.6	260	-0.0303 ± 0.0003	4000 ± 20	1.1698 ± 0.0008	32	84	3.2	8.8
	−2	−1	1.0	200	0.0461 ± 0.0007			36	68	12.7	22.5
4566474	0	1	0.6	280	-0.0312 ± 0.0006	4130 ± 10	1.2345 ± 0.0007	29	76	3.2	9.0
	−2	−1	1.0	570	0.0435 ± 0.0004			14	41	7.3	15.1
4585982	0	1	0.6	180	-0.0249 ± 0.0003	3370 ± 20	1.3924 ± 0.0009	39	96	3.9	10.1
	−2	−1	0.8	130	0.030 ± 0.001			40	87	13.5	28.7
4672176	0	1	0.4	200	-0.0398 ± 0.0005	4280 ± 20	1.748 ± 0.001	24	67	3.9	11.2
	−2	−1	0.7	290	0.0723 ± 0.0004			10	46	8.0	24.6
4758316	0	1	0.6	380	-0.0395 ± 0.0004	4470 ± 20	1.2445 ± 0.0009	23	61	2.7	7.5
	−2	−1	1.0	820	0.042 ± 0.001			12	23	7.3	10.2
4774208	0	1	0.4	190	-0.0427 ± 0.0005	4340 ± 20	1.834 ± 0.001	29	57	5.2	10.1
	−2	−1	0.6	290	0.0751 ± 0.0004			10	44	8.3	25.0
4843037	0	1	0.5	180	-0.0320 ± 0.0003	3910 ± 20	1.627 ± 0.001	31	74	4.4	11.0
	−2	−1	0.7	330	0.0604 ± 0.0004			12	51	7.5	23.0
4857064	0	1	1.1	570	-0.0206 ± 0.0002	3832 ± 9	0.5738 ± 0.0004	39	102	1.7	5.1
	−2	−1	2.3	740	0.010 ± 0.001			37	60	7.6	10.2
4859790	0	1	0.5	240	-0.0358 ± 0.0004	4550 ± 20	1.4584 ± 0.0007	28	64	4.1	9.5
	−2	−1	0.8	320	0.0611 ± 0.0004			10	60	7.3	27.9
5040435	0	1	0.5	190	-0.0296 ± 0.0004	4070 ± 30	1.440 ± 0.001	34	77	4.4	10.2
	−2	−1	0.8	280	0.073 ± 0.004			29	40	12.6	16.7
5114382	0	1	0.7	230	-0.0234 ± 0.0002	4110 ± 30	1.140 ± 0.001	46	81	4.7	8.6
	−2	−1	1.1	510	0.057 ± 0.002			21	43	8.5	14.6
5294571	0	2	0.2	100	-0.0318 ± 0.0004	4150 ± 20	1.6421 ± 0.0009	35	62	2.6	4.7
	0	1	0.5	200	-0.0383 ± 0.0004			31	62	4.7	9.5
	−2	−1	0.7	250	0.0620 ± 0.0004			16	53	9.2	25.4
5391059	0	1	0.4	190	-0.0419 ± 0.0004	4210 ± 20	1.796 ± 0.001	28	59	4.7	10.0
	−2	−1	0.7	340	0.0710 ± 0.0002			11	41	8.1	22.3
5476854	0	1	1.0	410	-0.0183 ± 0.0004	4060 ± 10	0.6647 ± 0.0004	54	92	3.1	5.4
	−2	−1	1.9	630	0.0281 ± 0.0006			30	65	7.6	13.0

Table 1 – *continued*

| KIC	k	m	$\langle P \rangle$ d	$\langle \Delta P \rangle$ s	mean Σ d/d	Π_0 s	f_{rot} d^{-1}	n min	max	s min	max
5640438	0	1	0.7	370	-0.0276 ± 0.0003	4230 ± 20	0.9788 ± 0.0005	35	73	3.1	6.8
	−2	−1	1.2	390	0.0376 ± 0.0003			14	81	6.9	23.7
5706866	0	1	0.6	180	-0.027 ± 0.001	3610 ± 20	1.218 ± 0.001	60	90	5.8	9.3
	−2	−1	1.1	610	0.0342 ± 0.0004			15	37	7.2	12.1
5708550	0	1	0.9	360	-0.0233 ± 0.0005	3840 ± 10	0.7911 ± 0.0006	40	99	2.5	6.7
	−2	−1	1.7	800	0.010 ± 0.001			16	40	6.6	9.7
5721632	0	1	0.4	320	-0.0479 ± 0.0006	4371 ± 8	1.6969 ± 0.0009	17	53	2.7	9.0
	−2	−1	0.7	220	0.0696 ± 0.0004			24	43	12.9	22.5
	−1	−1	1.9	4270	0.094 ± 0.001			24	42	2.6	3.2
5801556	0	2	0.3	230	-0.0401 ± 0.0007	4240 ± 20	1.2186 ± 0.0008	19	55	1.0	3.2
	0	1	0.6	230	-0.042 ± 0.002			43	69	4.9	7.8
	−2	−1	1.1	740	0.0335 ± 0.0007			12	29	7.1	11.3
5984615	0	1	0.8	240	-0.0235 ± 0.0002	3820 ± 20	0.9892 ± 0.0007	47	101	3.8	8.5
	−2	−1	1.3	530	0.0368 ± 0.0008			20	61	7.0	16.4
6048255	0	1	0.6	170	-0.0252 ± 0.0002	3750 ± 30	1.3748 ± 0.0009	43	94	4.9	11.1
	−2	−1	0.8	130	0.0374 ± 0.0005			40	76	14.9	27.6
6291473	0	2	0.2	110	-0.0329 ± 0.0004	5770 ± 40	1.671 ± 0.001	20	63	2.1	7.3
	0	1	0.5	210	-0.0342 ± 0.0004			26	57	5.6	13.0
	−2	−1	0.7	310	0.11 ± 0.02			22	29	15.1	19.9
6301745	0	1	0.3	210	-0.0495 ± 0.0007	4210 ± 40	2.297 ± 0.002	22	42	4.8	9.3
	−2	−1	0.5	110	0.0672 ± 0.0005			22	47	15.7	32.1
6468987	0	1	0.5	230	-0.035 ± 0.001	4020 ± 50	1.551 ± 0.002	29	64	4.0	9.1
	−2	−1	0.7	190	0.07 ± 0.01			37	45	16.6	20.2
6696689	0	1	0.7	180	-0.0239 ± 0.0002	3830 ± 20	1.1057 ± 0.0006	51	104	4.7	9.9
	−2	−1	1.0	190	0.0347 ± 0.0004			44	79	13.2	23.6
6806005	0	1	0.6	240	-0.0307 ± 0.0006	4000 ± 20	1.3235 ± 0.0008	34	71	4.0	8.5
	−2	−1	0.9	380	0.0501 ± 0.0004			13	60	7.2	22.3
6923424	0	2	0.2	80	-0.0398 ± 0.0005	4230 ± 30	2.023 ± 0.002	22	74	2.0	7.0
	0	1	0.4	240	-0.0496 ± 0.0006			16	55	3.0	10.7
	−2	−1	0.5	80	0.0494 ± 0.0007			31	59	19.1	35.5
7039007	0	1	0.7	290	-0.0300 ± 0.0005	3970 ± 20	1.039 ± 0.001	45	74	4.1	6.9
	−2	−1	1.2	650	0.0257 ± 0.0007			20	35	7.9	11.1
7137351	0	1	0.6	230	-0.0329 ± 0.0002	3820 ± 10	1.2129 ± 0.0009	35	88	3.5	9.0
	−2	−1	1.0	550	0.0353 ± 0.0003			15	47	7.0	15.5
7436266	0	1	0.6	220	-0.0298 ± 0.0003	4070 ± 10	1.2897 ± 0.0007	31	90	3.5	10.4
	−2	−1	0.9	370	0.0487 ± 0.0005			9	67	6.8	24.7
7538181	0	1	0.6	260	-0.0335 ± 0.0008	3840 ± 20	1.1939 ± 0.0009	40	72	4.0	7.4
	−2	−1	1.1	580	0.0405 ± 0.0009			13	40	7.1	13.5
7551589	0	1	0.6	180	-0.0292 ± 0.0003	3820 ± 20	1.3182 ± 0.0009	42	90	4.6	10.2
	−2	−1	0.9	490	0.0460 ± 0.0008			14	45	7.3	16.2
7583663	0	1	0.6	280	-0.0307 ± 0.0005	4220 ± 20	1.1608 ± 0.0007	37	70	4.0	7.7
	−2	−1	1.0	180	0.0385 ± 0.0004			38	69	13.8	24.0
7596250	0	1	0.6	350	-0.0346 ± 0.0005	4290 ± 20	1.1876 ± 0.0007	27	66	2.9	7.5
	−2	−1	1.0	590	0.0502 ± 0.0006			16	37	7.9	13.7
7621649	0	1	0.8	510	-0.0270 ± 0.0002	3990 ± 10	0.7745 ± 0.0004	30	80	1.9	5.5
	−2	−1	1.6	530	0.0307 ± 0.0004			28	62	8.0	13.9
7778826	0	1	0.4	270	-0.0510 ± 0.0004	4020 ± 30	2.060 ± 0.002	20	47	3.6	9.0
	−2	−1	0.6	330	0.0792 ± 0.0007			8	40	7.1	23.4
8198031	0	1	0.4	170	-0.0375 ± 0.0005	4140 ± 20	1.855 ± 0.001	25	74	4.3	12.9
	−2	−1	0.6	370	0.0767 ± 0.0005			12	38	8.2	20.6
8263970	0	1	0.4	170	-0.0393 ± 0.0006	4180 ± 20	1.946 ± 0.001	21	76	3.7	14.3
	−2	−1	0.6	470	0.0786 ± 0.0001			10	29	8.0	17.2
8316105	0	1	0.6	300	-0.0354 ± 0.0005	4240 ± 20	1.3352 ± 0.0008	24	70	2.9	9.0
	−2	−1	0.9	420	0.0539 ± 0.0004			15	50	7.9	20.2
8330056	0	1	0.4	170	-0.0393 ± 0.0005	4100 ± 20	1.913 ± 0.001	26	68	4.4	11.9
	−2	−1	0.6	390	0.0731 ± 0.0006			9	42	7.3	23.4
8351778	0	2	0.3	260	-0.0361 ± 0.0007	3760 ± 20	0.9645 ± 0.0009	29	57	1.1	2.3
	0	1	0.7	320	-0.0262 ± 0.0002			40	84	3.1	6.9
	−2	−1	1.2	130	0.026 ± 0.002			71	85	18.4	21.8
8375138	0	1	0.5	200	-0.0376 ± 0.0004	4150 ± 20	1.6421 ± 0.0009	29	65	4.3	9.9
	−2	−1	0.7	400	0.0659 ± 0.0002			8	42	7.0	20.6
8973529	0	2	0.3	140	-0.0308 ± 0.0003	4000 ± 20	1.204 ± 0.001	22	90	1.1	4.8
	0	1	0.6	320	-0.0325 ± 0.0003			22	83	2.2	9.0
	−2	−1	0.9	220	0.066 ± 0.002			38	59	13.2	20.0

Table 1 – *continued*

KIC	k	m	⟨P⟩ d	⟨ΔP⟩ s	mean Σ d/d	Π₀ s	f_rot d⁻¹	n min	n max	s min	s max
9210943	0	1	0.4	300	−0.043 ± 0.001	4310 ± 20	1.703 ± 0.001	24	45	3.9	7.4
	−2	−1	0.7	410	0.0693 ± 0.0005			9	40	7.3	20.8
9419182	0	2	0.3	180	−0.0385 ± 0.0007	4190 ± 10	1.1510 ± 0.0006	27	62	1.4	3.3
	0	1	0.7	250	−0.0282 ± 0.0003			37	82	3.9	8.9
	−2	−1	1.1	470	0.0434 ± 0.0006			15	61	7.0	20.9
9480469	0	1	0.5	160	−0.032 ± 0.001	4330 ± 20	1.554 ± 0.001	40	72	6.1	11.2
	−2	−1	0.8	400	0.0647 ± 0.0002			11	44	7.7	21.1
9594007	0	2	0.2	130	−0.0428 ± 0.0005	3980 ± 20	1.671 ± 0.001	27	53	1.9	3.9
	0	1	0.5	200	−0.0366 ± 0.0007			22	80	3.2	12.2
	−2	−1	0.7	160	0.0550 ± 0.0007			25	61	12.4	28.6
9594100	0	2	0.3	240	−0.0370 ± 0.0005	41 10 ± 20	1.2159 ± 0.0009	23	47	1.2	2.6
	0	1	0.6	260	−0.0313 ± 0.0003			31	77	3.3	8.5
	−2	−1	1.0	320	0.03 ± 0.01			31	46	11.6	16.5
9652302	0	1	0.8	330	−0.021 ± 0.001	3710 ± 20	0.9147 ± 0.0006	48	88	3.5	6.9
	−2	−1	1.3	270	0.061 ± 0.003			47	66	11.9	16.0
9716563	0	2	0.4	210	−0.0258 ± 0.0002	3860 ± 10	0.9081 ± 0.0008	29	83	1.0	3.2
	0	1	0.7	570	−0.0307 ± 0.0004			23	67	1.6	5.2
	−2	−1	1.5	820	0.0119 ± 0.0007			17	26	7.0	8.3
9962653	0	1	0.4	200	−0.0410 ± 0.0004	4150 ± 20	1.763 ± 0.001	27	61	4.3	10.0
	−2	−1	0.7	290	0.0686 ± 0.0002			10	49	8.0	25.6
10423501	0	1	0.8	480	−0.0271 ± 0.0003	4240 ± 20	0.8420 ± 0.0006	29	76	2.1	6.0
	−2	−1	1.4	480	0.0339 ± 0.0009			36	50	10.2	13.2
10481462	0	1	0.4	210	−0.052 ± 0.001	4410 ± 30	2.208 ± 0.002	17	52	3.7	11.6
	−2	−1	0.5	440	0.0973 ± 0.0005			10	25	8.7	17.6
10818266	0	1	0.4	250	−0.0468 ± 0.0005	4290 ± 20	1.849 ± 0.001	18	56	3.1	10.0
	−2	−1	0.7	460	0.0772 ± 0.0003			10	33	7.9	18.7
10859386	0	1	0.4	290	−0.045 ± 0.001	4420 ± 30	1.813 ± 0.001	23	44	4.1	8.2
	−2	−1	0.6	120	0.062 ± 0.002			34	51	19.1	28.7
11256244	0	1	0.8	300	−0.0242 ± 0.0002	3930 ± 10	0.9622 ± 0.0006	45	84	3.7	7.1
	−2	−1	1.3	640	0.026 ± 0.001			22	44	7.7	12.3
11466960	0	1	0.6	210	−0.0324 ± 0.0004	4240 ± 10	1.3874 ± 0.0007	29	82	3.7	10.9
	−2	−1	0.9	400	0.0560 ± 0.0004			12	52	7.3	21.7
11519475	0	1	0.5	190	−0.0333 ± 0.0003	4070 ± 30	1.576 ± 0.001	29	75	4.1	10.8
	−2	−1	0.7	200	0.0550 ± 0.0008			30	49	13.8	22.2
11550154	0	2	0.2	90	−0.0409 ± 0.0003	4140 ± 20	2.017 ± 0.001	24	58	2.2	5.5
	0	1	0.4	140	−0.0367 ± 0.0006			23	79	4.3	14.9
	−2	−1	0.6	320	0.0794 ± 0.0005			10	39	8.1	23.2
11571757	0	2	0.4	220	−0.048 ± 0.002	6130 ± 30	1.0291 ± 0.0005	28	51	1.9	3.6
	0	1	0.8	240	−0.0223 ± 0.0006			31	104	4.2	17.7
	−2	−1	1.1	380	0.064 ± 0.002			25	45	11.8	20.2
11657371	0	1	0.4	250	−0.0436 ± 0.0007	3900 ± 40	1.848 ± 0.002	26	51	4.1	8.4
	−2	−1	0.6	60	0.077 ± 0.002			49	70	25.0	35.5
11775251	0	1	0.6	190	−0.0327 ± 0.0002	4040 ± 20	1.4115 ± 0.0007	31	88	3.9	11.0
	−2	−1	0.8	350	0.0572 ± 0.0007			14	48	8.2	19.6
11907454	0	1	0.6	240	−0.0368 ± 0.0006	4200 ± 20	1.3387 ± 0.0006	30	74	3.7	9.1
	−2	−1	0.9	270	0.0543 ± 0.0001			10	66	7.8	26.0
12066947	0	1	0.4	140	−0.0399 ± 0.0009	4170 ± 30	2. 159 ± 0.002	25	64	5.1	13.1
	−2	−1	0.5	270	0.0804 ± 0.0005			11	44	8.4	28.0
12170722	0	2	0.2	100	−0.0362 ± 0.0004	4270 ± 20	1.702 ± 0.001	22	77	1.8	6.4
	0	1	0.5	150	−0.0334 ± 0.0002			33	79	5.4	13.0
	−2	−1	0.7	390	0.0715 ± 0.0005			10	38	7.9	19.9
12303838	0	1	0.6	250	−0.0329 ± 0.0004	4160 ± 20	1.3301 ± 0.0007	33	70	4.0	8.8
	−2	−1	0.8	190	0.0483 ± 0.0006			27	68	11.2	26.3
12520187	0	1	0.4	310	−0.0568 ± 0.0006	4650 ± 50	1.872 ± 0.002	18	44	3.4	8.4
	−2	−1	0.6	90	0.062 ± 0.003			29	51	20.2	31.4

version of the *Kepler* Stellar Properties Catalog (KSPC DR25; Mathur et al. 2017). The luminosity *L* was calculated by Murphy et al. (2019) using the *Gaia* Data Release 2 (DR2) parallax (Gaia Collaboration et al. 2016, 2018a,b,c). Murphy et al. (2019) compiled a catalogue of 1986 *Kepler* δ Scuti strs, which we added these to

Fig. 5 as the grey dots. We also added the observational instability strip, defined by Murphy et al. (2019), based on the δ Sct pulsator fraction, shown in Fig. 5 as purple solid lines. The black solid lines represent the theoretical instability strip of γ Dor stars, which was calculated by Dupret et al. (2005) and Bouabid et al. (2013). Our
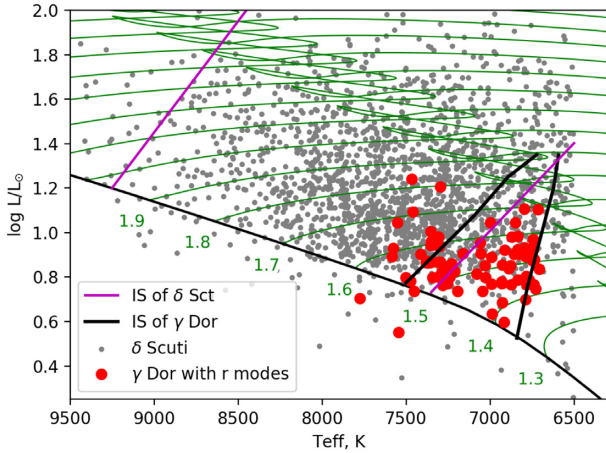
Figure 5. The δ Scuti and γ Doradus stars on the HR diagram. The grey dashed dots are the δ Scuti stars. The red circles are the 78 γ Dor stars with Rossby modes in this paper. The green numbers are the masses of the evolutionary tracks. The instability strips of δ Scuti and γ Dor are shown by the purple and black solid lines.

evolutionary tracks were computed in MESA (Paxton et al. 2011), v10108. Our 'standard model' at each mass had $X = 0.71$, $Z = 0.014$ (corresponding to [M/H] = 0.036), $\alpha_{MLT} = 1.8$, exponential core overshooting of 0.015 Hp, exponential H-burning shell over- and undershooting of 0.015 Hp, exponential envelope overshooting of 0.025 Hp, diffusive mixing $\log D_{mix} = 0$ (in $cm^{-2}s^{-1}$), OPAL opacities, and the Asplund et al. (2009) solar abundance mixture. The parameters were chosen to be close to solar values, in agreement with observed metallicity values from spectroscopy and with the values from previously published asteroseismic modelling studies of g-mode pulsators (e.g. Schmid & Aerts 2016; Momberg et al. 2019).

Fig. 5 shows that most stars (both δ Scuti and γ Dor stars) are located above the ZAMS. δ Scuti stars show more spread than γ Dor stars and the latter generally have lower temperatures and lower luminosities. The distribution of γ Dor stars is wider than theoretically predicted, especially beyond the blue edge, which shows the inconsistency to the theoretical instability strip and challenges the current stellar model. However, the conclusions are still in debate since the uncertainty of T_{eff} is ∼250 K. More accurate spectroscopic values for T_{eff} are required to confirm the location of the γ Dor instability strip. The effect of binarity also needs to be considered carefully.

The γ Dor stars in this paper are mostly confined to the low-luminosity region near the ZAMS. This makes sense, because r modes are caused by rotation, which slows down with stellar evolution after the ZAMS. Young stars rotate faster and are more likely to exhibit r modes in the detection region (0.2–2 d); hence, we find more r modes in stars near the ZAMS. We do not take the possibility of pre-main-sequence γ Dor stars into account, although they were predicted by Bouabid et al. (2011). Another factor is that the low-mass stars enter the γ Dor instability strip at the beginning of main sequence and stay in it longer than high-mass stars. Hence, they are more likely to be observed. This also explains why γ Dor stars generally show smaller T_{eff} and $\log L$.

4.2 Period spacings

Our sample is large enough to show some general features for the g and r modes of γ Dor stars. The periodograms of r- and g-mode stars show two main groups of modes. At shorter periods are the

$l = 1$, $m = 1$ g modes and at longer periods are the $k = -2$, $m = -1$ r modes. Although the asymptotic spacing Π_0 of γ Dor is typically around 4200 s (Van Reeth et al. 2016), the period spacings vary greatly due to the rapid rotation, from a few hundred seconds to 1000 s, but in each star, it is similar among both the g and r modes. The period spacings of g modes decrease quasi-linearly with period, which is the rotational effect for prograde g modes (Bouabid et al. 2013; Ouazzani et al. 2017). However, the period spacings of r modes increase linearly with periods, and sometimes show a drop at the long-period end (see e.g. Fig. 1h and Saio et al. 2018a).

We found that almost all the r modes have the quantum numbers of $k = -2$, $m = -1$, although other numbers were also reported by Saio et al. (2018a). The reason is likely that the period spacing of $k = -2$, $m = -1$ modes is easily detected in *Kepler* data, compared to tens of seconds of $k = -2$, $m = -2$ modes or several thousands of seconds of $k = -1$, $m = -1$ modes. Also, $k = -2$, $m = -2$ modes generally have larger amplitudes (Saio et al. 2018a).

KIC 5721632 is the only star that shows convincing $k = -1$, $m = -1$ r modes. Fig. 6 shows its amplitude periodogram, period spacing patterns and the échelle diagram. The rotation rate is $f_{rot} = 1.6969 \pm 0.0009 d^{-1}$ and the asymptotic spacing is $\Pi_0 = 4371 \pm 8$ s, as shown in Figs 7 and 8. In the lower left-hand panel of Fig. 8, the asymptotic spacing negatively correlates with the rotation rate, since the fitting is dominated by the retrograde $k = -1$, $m = -1$ r modes. The period spacing of the $k = -1$, $m = -1$ pattern keeps increasing from 2000 s to 8000 s, showing different feature from $k = -2$, $m = -1$ Rossby modes. We also noticed that there are two stars, KIC 5721610 and KIC 5721628, which are close to KIC 5721632 on the sky within 6 arcsec. We evaluated the light curve of KIC 5721632 for contamination from those two stars. The power spectra of those two stars were calculated and we do not find any g- or r-mode oscillations. So the light curve of KIC 5721632 was not contaminated and the $k = -1$, $m = -1$ Rossby modes are most likely real.

4.3 Asymmetric amplitude envelopes

Saio et al. (2018a) used the visibility over the square root of kinetic energy (Vis/√KE) to calculate the amplitude of r modes. They showed that the $k = -2$, $m = -1$ modes have the highest amplitudes compared to other r modes and the amplitude envelope is strongly asymmetric, with a steep low-period side. The relatively large amplitude is helpful to identify the $k = -2$, $m = -1$ r modes. We also observed the asymmetric amplitude envelope in some stars, e.g. Fig. 1(g), where the amplitude increases rapidly at $P \sim 0.94$ d and drops slowly after that. However, it shows a lot of small peaks and several strong peaks before the predicted amplitude rise. For some other stars, the r-mode patterns do not show the predicted amplitude envelope, e.g. Fig. 6(g). A more complete theory may be needed to address this observation.

4.4 Periods of Rossby modes

Fig. 9 shows the period relation between the $l = 1$, $m = 1$ g modes and $k = -2$, $m = -1$ r modes. The black points are the means of the periods of each pattern, which are the averaged value of all the detected periods. Since the period spacing changes with period, the means of periods are not the centre of patterns. The grey lines are not error bars, they show the period ranges of g and r modes, respectively. We found that the means of the periods of g and r
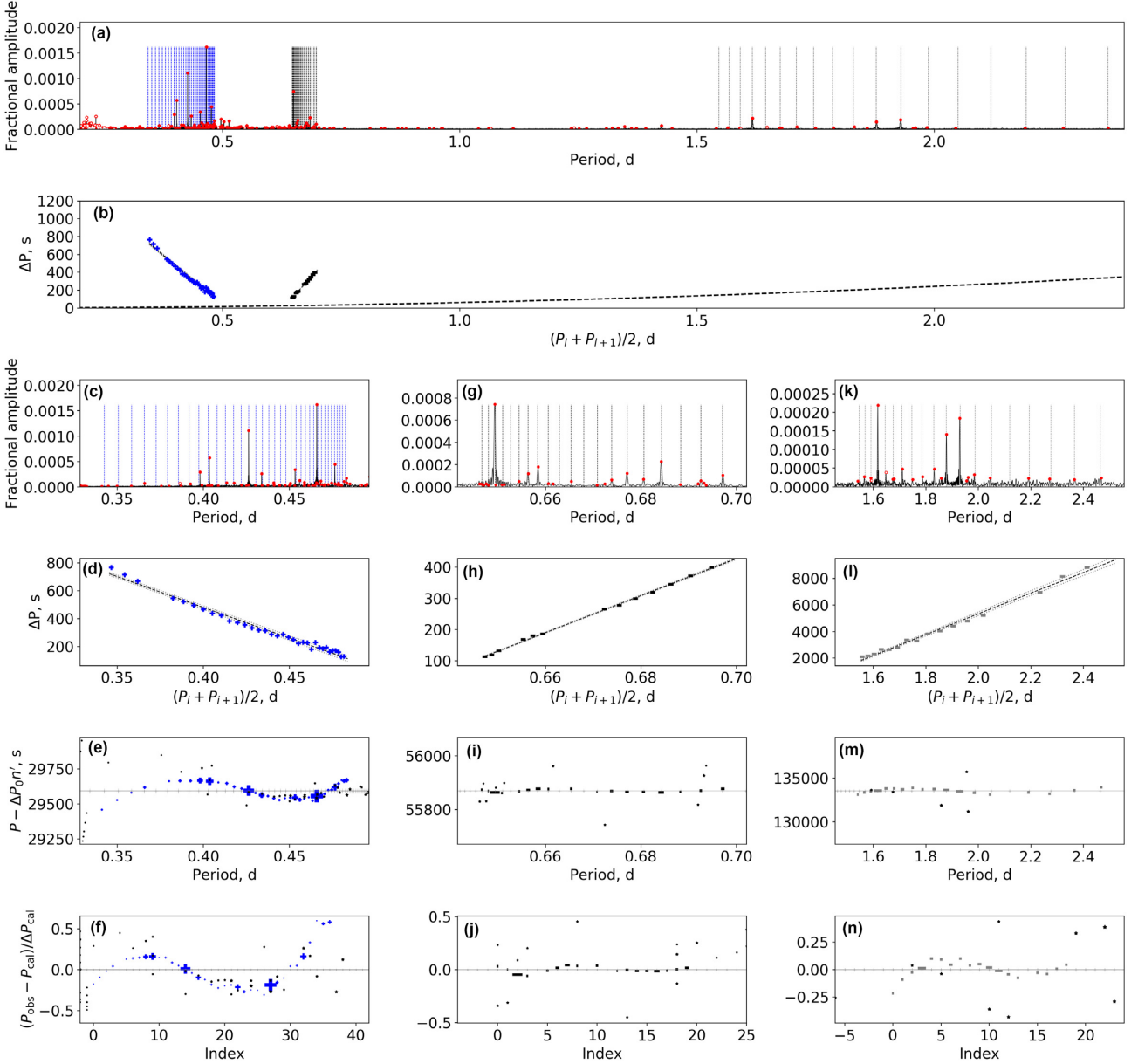
Figure 6. Period spacings and the sideway échelle diagrams of KIC 5721632. Panels (k)–(n) show the $k = -1$, $m = -1$ r-modes pattern. The period spacings are too large to display in panel (b).
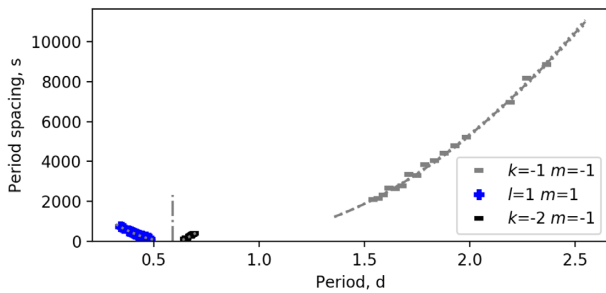
Figure 7. The TAR fit of KIC 5721632.

modes are related by a linear fit with

$$\langle P_{\mathrm{r}} \rangle = (2.06 \pm 0.05) \langle P_{\mathrm{g}} \rangle - (0.25 \pm 0.03) \text{ d}, \tag{10}$$

where $\langle P_{\mathrm{r}} \rangle$ is the means of the periods of r modes and $\langle P_{\mathrm{g}} \rangle$ is the one of g modes. The linear fit has the slope 2.06 ± 0.05 and the intercept is $-0.25f \pm 0.03$ d, shown as the grey dashed line. Since the means of periods must be located within the period ranges, to calculate the uncertainties of the linear fit, we used the period ranges as 3σ to make perturbations of the data.

Based on the slope and the small intercept, we conclude the r-mode periods are close to twice the g-mode periods. The relationship helps guide a search for the r modes in more stars, if the amplitudes of r mode are not obvious.
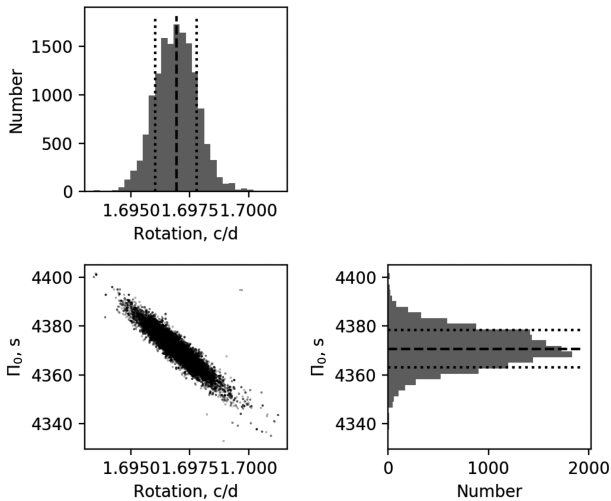
Figure 8. The posterior distributions of KIC 5721632. The best model has $\Pi_0 = 4371 \pm 8$ s and $f_{\rm rot} = 1.6969 \pm 0.0009$ d^{-1}. The fitting is dominated by the retrograde $k = -1$, $m = -1$ r modes, hence Π_0 shows a negative correlation with $f_{\rm rot}$ in the lower left-hand panel.

4.5 Slope–period relation

Fig. 10 shows the slope versus period relation of 82 γ Dor stars. The x-axis is the mean of the periods, which is the same as shown in Fig. 9. The y-axis is the slope assuming the period spacing changes quasi-linearly with the period, fitted by equation (3). Different markers and colours stand for different modes. The points cluster into several groups and display different trends based on their quantum numbers. For the $l = 1$, $m = 1$ g modes (blue triangles), the slopes are negative and increase towards zero with the mean period, with a large spread. The points of the $l = 2$, $m = 2$ g modes (green stars) lie on the left of the dipole g modes with similar slopes. Finally, the slopes of r-mode patterns (red circles) are larger than zero, and show a clear decreasing trend with the mean period.

To compare these results with theory, we calculated period spacing patterns from the TAR. The range of Π_0 was 3600 to 5600 s with step of 200 s, and $f_{\rm rot}$ ranged from 0 to 4 d^{-1}. For r modes, we averaged over overtones with $10 \leq n \leq 30$. Results are shown as red lines in Fig. 10, with less transparency corresponding to larger Π_0. Considering the mean of periods and slope change with the radial order region for the g modes, we measured the slope of calculated patterns in two regions: $10 \leq n \leq 30$ and $30 \leq n \leq 50$, showing these as blue and cyan lines in Fig. 10. Each solid line in Fig. 10 has the same Π_0 and the same n region along its length, but the rotation rate increases from right to left. We use the darker lines to represent larger Π_0. The lighter the curve is, the smaller its Π_0 is.

From the calculated curves, we find that if we want to cover the g-mode observational points, curves that span different n are needed. However, the features of different radial orders differ dramatically. The blue curves with n from 10 to 30 generally show smaller mean periods and steeper slopes (reaching -0.09 when the mean period is at 0.2 d). The cyan curves with radial order from 30 to 50 have larger mean periods and their slopes only reach -0.05 when the mean period arrives at 0.2 d. They show an overlapping area between 0.4 and 0.6 d.
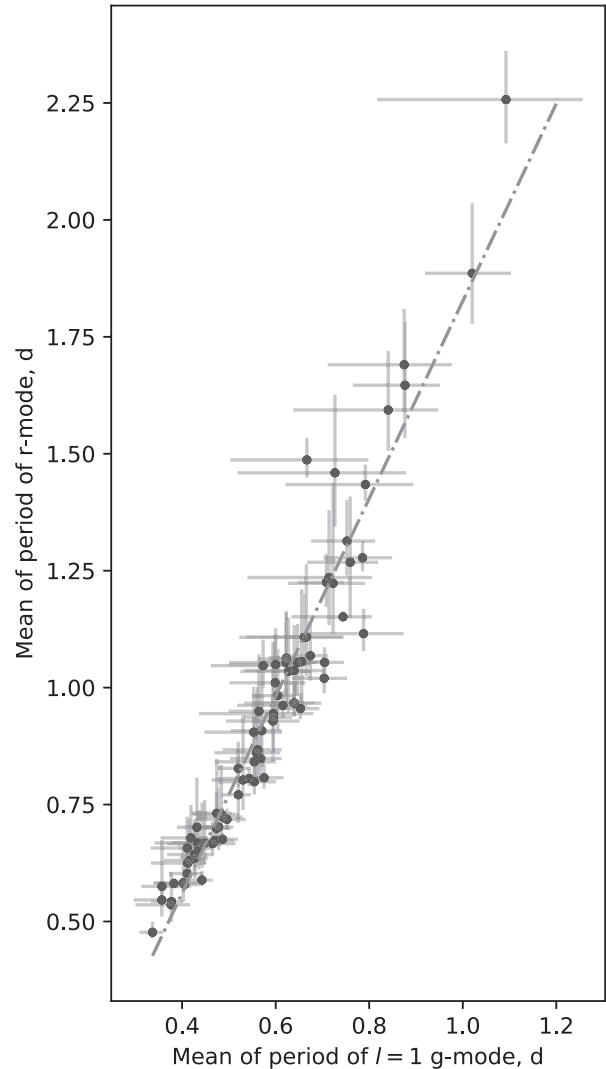
For the r modes, the period spacing decreases at the long periods due to the rapid change of the eigenvalue λ. This affects the

Figure 9. The mean period relation between the $l = 1$ $m = 1$ g-mode patterns and the $k = -2$, $m = -1$ r-mode patterns. The black dots show the means of the periods in each pattern. Since the period spacing changes, the means of the periods are not in the centre. The grey solid lines are the period ranges. The dashed–dotted line is the linear fit.

calculated slope value but is not common in the observations, so we only adopted the periods before the spacing drop, which is caused by the rapid change of the eigenvalue λ (see Fig. 2). Only the results with $10 \leq n \leq 30$ and $0.7\,{\rm d}^{-1} \leq f_{\rm rot} \leq 4\,{\rm d}^{-1}$ were used, since this parameter space covered the observations well (red lines in Fig. 10). The radial order range from 10 to 30 of r modes can explain the observational data. The correlation between the slope and the mean period spacing is caused by the rotation rate. The more rapidly the star rotates, the shorter the mean period and the larger the slope. In Fig. 10, we marked six outliers, which are caused by the systematic influence of dips in the pattern. The measurement of the slope is affected strongly by the intrinsic dips or fluctuations, which reflects the limit of the linear assumption in equation (3).

Fig. 10 also shows the calculated relationships between the slope and the mean period (as a function of rotation), for several discrete values of asymptotic spacing Π_0. It can guide the pattern identification for other γ Dor stars. If a period spacing pattern does
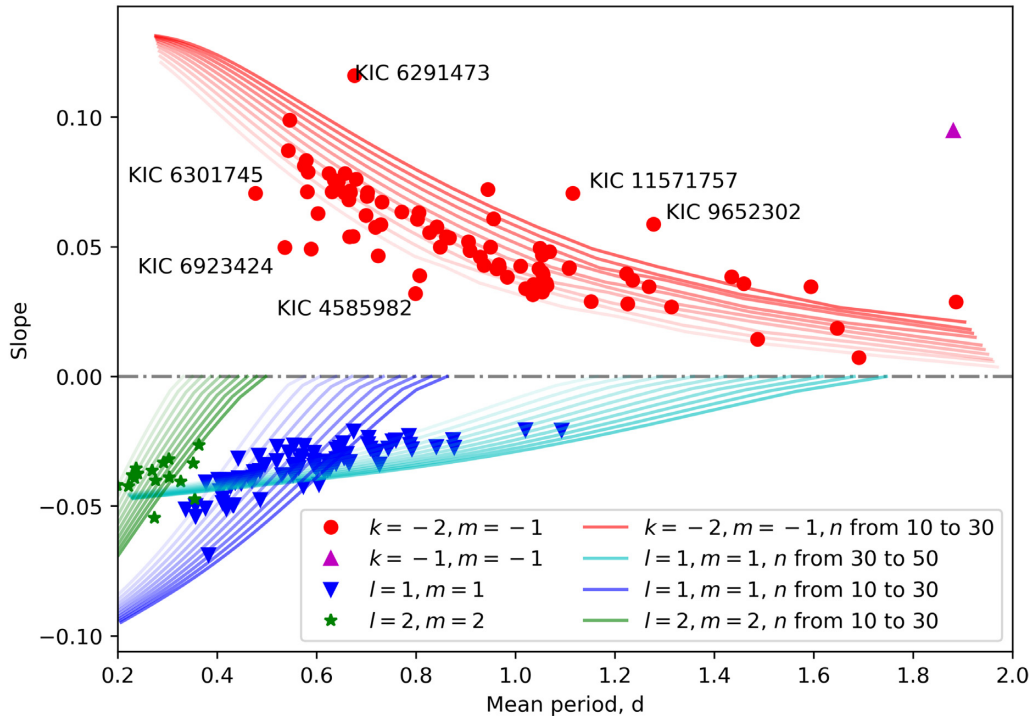
Figure 10. The slope–period relation with theoretical curves for r modes (positive slopes) and g modes (negative slopes). We calculated the theoretical period spacing slopes in two radial order regions: 10–30 and 30–50, respectively. A given curve has the same Π_0 and n region but the rotation rate increases from right to left. The transparencies of curves represent the Π_0, which is from 360 s to 5400 s with step of 200 s. The lighter, the smaller the Π_0 is. Curves with different colours have different radial order ranges and different quantum numbers.

not follow the relation, several possibilities should be considered: the pattern includes a partly observed dip (e.g. Li et al. 2019); the star is an SPB star, which generally has larger Π_0 and steeper slope (Pápics et al. 2017); the period spacing identification is misled by missing peaks.

4.6 Asymptotic spacing and rotation

The TAR fit gives the near-core rotation rate f_{rot} and the asymptotic spacing Π_0 for every star. Fig. 11 shows the distributions and correlation for these two parameters. The uncertainties of the histograms are square roots of the histogram heights, assuming they are Poisson distributed. Most stars have asymptotic spacings between 3600 and 4500 s (Fig. 11a), which is consistent with Van Reeth et al. (2016). The asymptotic spacing decreases with evolution, hence is considered as an indicator of stellar age. However, it is also affected by other physical parameters, such as metallicity, mixing length and convective core overshooting. Fig. 11(c) is the distribution of the rotation rate f_{rot}. The slowest rotator is KIC 4857064 with $f_{rot} = 0.5738 \pm 0.0004\,\mathrm{d}^{-1}$ and the fastest one is KIC 6301745 with $f_{rot} = 2.297 \pm 0.002\,\mathrm{d}^{-1}$. Most stars rotate between 1 and 2 d^{-1}, much faster than the Sun but typical for A to F stars (Royer, Zorec & Gómez 2007).

Fig. 11(b) displays the lack of correlation between Π_0 and f_{rot}. Most stars have the asymptotic spacings around 4000 s and the rotation rates from 1 to 2 d^{-1}, showing typical ranges for γ Dor stars. We found two outliers, KIC 11571757 and KIC 6291473, whose period spacing patterns are seen in the online supplementary material. The asymptotic spacings of KIC 11571757 and KIC 6291473 are 6130 ± 30 and 5770 ± 40 s, respectively. These are obviously

higher than the range of γ Dor stars but are typical of SPB stars (5600 to 15400 s, see Pápics et al. 2017). However, their effective temperatures are too low to be B-type stars. These two stars may be at the beginning of the main sequence hence show large asymptotic spacings, or the identifications of period spacing patterns are misled by missing peaks.

We also notice that a gap at $f_{rot} \sim 1.5\,\mathrm{d}^{-1}$ separates the data points into two groups. The f_{rot} distribution in Fig. 11(c) shows two peaks around 1.2 and 1.8 d^{-1}. We tried several different bins and the gap is still apparent. Whether it is a real effect or caused by the limited numbers of the sample is still an open question.

We do not find any strong correlation between Π_0 or f_{rot} and T_{eff}, which is colour coded in Fig. 11. Both rotation and Π_0 are expected to decrease with evolution and effective temperature, but the processes are presumably affected by many other parameters, such as the initial rotation rate, the mechanism of angular momentum transfer, or extra diffusion. It seems that 82 stars are still too few to reveal a correlation. As shown in Fig. 5, most stars in our sample are close to the ZAMS. The range of stellar ages in our sample may also be not long enough to show the correlation from the evolutionary effect. Also, more precise values of effective temperatures are still needed to confirm the theoretical prediction.

4.7 Rotation from core to surface

The rotation profile from the core to the surface is the key to understand the angular momentum transport and chemical mixing processes. As pointed out in Section 4.6, the g- and r-mode period spacings are used to constrain near-core rotation rates inside the stars. Several methods give the opportunity to measure the rotation
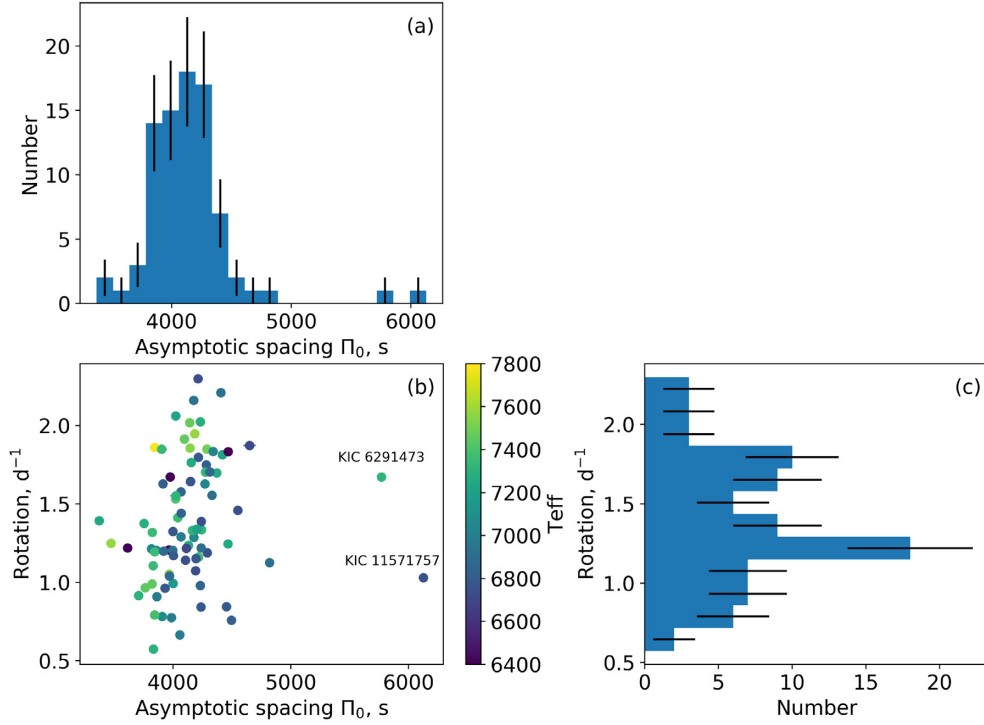
Figure 11. The asymptotic spacing Π_0 and the near-core rotation f_{rot}. The colour bar is the effective temperature. Uncertainties of histograms are the square roots of numbers, assuming they are Poisson distributed.

of the outer stellar envelope, such as p-mode splittings (e.g. Kurtz et al. 2014; Saio et al. 2015; Schmid & Aerts 2016), projected rotation velocity ($v \sin i$) (e.g. Murphy et al. 2016), rotational spot modulation (e.g. Degroote et al. 2011; García et al. 2014; McQuillan, Mazeh & Aigrain 2014; Balona 2017), and deducing surface rotation by tidal locking in binaries (e.g. Guo et al. 2017; Kallinger et al. 2017; Zhang et al. 2018). A signal caused by spots is common for low-mass stars with convective envelopes. However, only 10 per cent of intermediate- and high-mass stars show detectable magnetic fields based on Zeeman splitting (Donati & Landstreet 2009; Wade et al. 2016), which implies a lack of spot activity. Nevertheless, Van Reeth et al. (2018) detected rotational modulations from 8 stars among 68 γ Dor stars, whose detection percentage is consistent with the magnetic observation.

The signal of rotational modulation in frequency is located between g- and r-modes and we have searched for it in all stars. We follow the criteria reported by Van Reeth et al. (2018) to inspect the surface rotation. The criteria are (1) the S/N of the peak is larger than 4; (2) the second harmonic $2f$ is found; (3) the selected frequency is part of an isolated group of frequencies, since the lifetime of spot is assumed to be shorter than the *Kepler* data span; and (4) the peak should stand between g and r modes. We found six stars that have a signal of rotational modulation that satisfies all these conditions. Table 2 lists the near-core and surface rotation rates ($f_{rot,i}$ and $f_{rot,o}$) and their ratio. KIC 3341457 and KIC 7596250 are classified as eclipsing binaries or ellipsoidal variables (Kirk et al. 2016), whilst the modulations for the other three stars are likely caused by spots. Only KIC 3341457 has an obvious differential rotation. The other four stars are quasi-rigidly rotating, as their derived $f_{rot,i}$ and $f_{rot,o}$ values are close to each other.

Appendix B contains their periodograms. We use KIC 9716563 as an example. Fig. 12 displays the periodogram of KIC 9716563. The peaks at periods below 0.8 d belong to the $l = 1$, $m = 1$ g modes

Table 2. The surface modulation of 6 γ Dor tars. 'EB' means the star is a binary from Kirk et al. (2016). 'SPOT' means the surface modulation is caused by spots. $f_{rot,i}$ is the near-core rotation rate fitted by g- and r-mode period spacing patterns. $f_{rot,o}$ is the surface rotation rate from spot modulation.

KIC	Type	$f_{rot,i}$ d^{-1}	$f_{rot,o}$, d^{-1}	$f_{rot,i}/f_{rot,o}$
KIC 3341457	EB	1.859(1)	1.893(7)	0.982(4)
KIC 7596250	EB	1.1876(7)	1.185(4)	1.003(4)
KIC 7621649	SPOT	0.7745(4)	0.7802(6)	0.9928(9)
KIC 9652302	SPOT	0.9147(6)	0.910(2)	1.005(3)
KIC 9716563	SPOT	0.9081(9)	0.90(2)	1.01(2)
KIC 10423501	SPOT	0.8420(6)	0.841(4)	1.001(4)
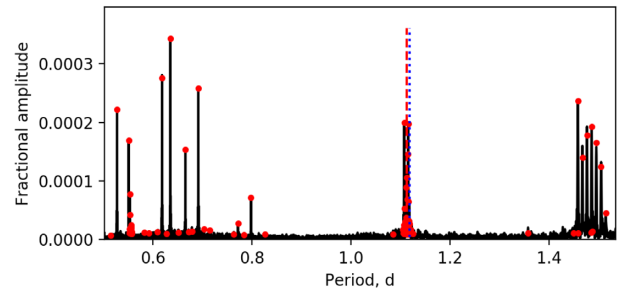
Figure 12. The pulsation and surface rotation of KIC 9716563. Three peak groups are seen. The peak groups at 1.11 d is the signal of the surface modulation. The blue dotted line (overlapped with the red dotted line) displays the near-core rotation, whilst the red dashed line shows the surface rotation, which is the mean of the peaks. The periods below 0.8 d are $l = 1$, $m = 1$ g modes, and the periods above 1.4 d are $k = -2$, $m = -1$ r modes.
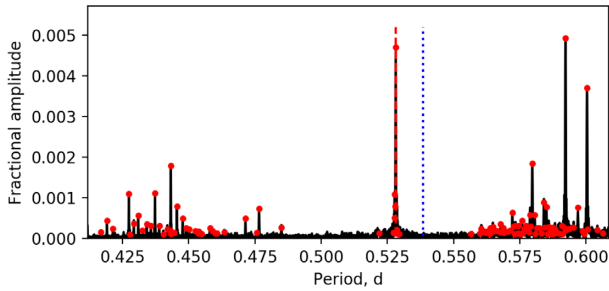
Figure 13. The pulsation and surface rotation of KIC 3341457. This star shows a large discrepancy between the near-core rotation period (blue dotted line) and the orbital period (red dashed line). It implies a radial differential rotation.

and the peaks at periods above 1.4 d are $k = -2$, $m = -1$ r modes. There is a region between g and r modes in which we did not find any extra peaks. However, a strong peak group appears at 1.11 d, which is roughly equal to the near-core rotation rate 1.102 ± 0.001 d. We identified this peak group as the surface modulation, which is likely to be caused by surface spot. The surface modulation shows multiple peaks, indicating the spot lifetime is shorter than the data span, the spot size varies with time, or there is latitude differential rotation. The amplitude caused by the spot is similar to the strongest g- and r-mode oscillations (∼0.2 per cent of the mean flux).

KIC 3341457 is the only star that shows differential rotation. It is identified as 'an ellipsoidal variable or a system with an uncertain classification' with orbital period of 0.5281792 d (Matijevič et al. 2012; Kirk et al. 2016). Fig. 13 displays the periodogram of KIC 3341457. The orbital effect generates a peak group at 0.528 d. However, the near-core rotation derived from the g and r modes is 0.538 d, 2 per cent longer than the surface rotation. Considering the short orbital period, the stellar surface is likely tidally locked hence this star has a non-uniform rotational profile.

KIC 7596250 is also identified as a binary, but its orbital period is equal to the near-core rotation period. So KIC 7596250 is rigidly rotating, assuming its surface is tidally locked.

Although spot activity is generally weak in intermediate-mass stars, it is still possible to find surface modulations in a few cases. Apart from the spot activity, binary effect also involves a signal corresponding to the orbital period that implies surface rotation, assuming the surface is tidally locked. According to our results and those from Van Reeth et al. (2018), most main-sequence stars have uniform rotation profiles, whilst the components in binary systems are more likely to be differentially rotating, due to the tidal locking effect. Many theoretical mechanisms can cause the differential rotation, such as the internal gravity waves (Aerts et al. 2018a), magnetic fields (e.g. Mathis & Zahn 2005; Prat et al. 2019), and tides (e.g. Lurie et al. 2017; Zhang et al. 2018). KIC 3341457 is an excellent star for modelling angular momentum transport mechanisms.

4.8 Radial order distribution

The radial orders of pulsations in a slow rotator can be estimated as the period divided by the period spacing, $P/\Delta P$, because of the asymptotic spacing in equation (6). However, rotation changes the period spacing, hence this becomes invalid for most γ Dor stars. We used the TAR fit results to get more accurate estimates of the radial orders. Fig. 14 displays the radial order distributions of the excited modes for the whole sample.
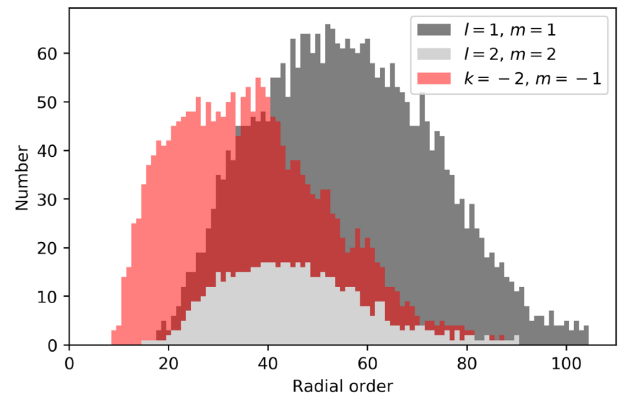
Figure 14. The distributions of radial orders. The black, white, and red areas stand for dipole, quadrupole g modes, and r modes.
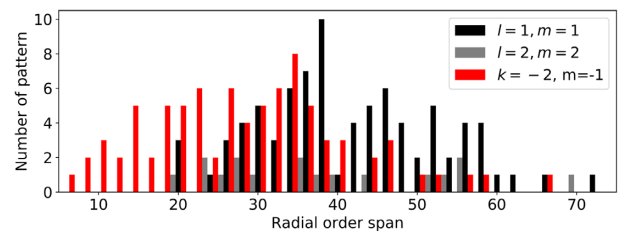
Figure 15. The radial order span of the g and r modes. Most of patterns show ∼30 radial order length. But several g-mode patterns show extremely long radial order spans, even up to 70.

For dipole g modes, the most likely radial order is ∼55. The distribution shows a spread with full width at half-maximum (FWHM) of ∼50. The lowest n is 18, whilst the highest one is 103. For quadrupole g-modes, the range in radial orders spans from 15 to 83 with FWHM of ∼30. The most frequent radial order is ∼40, slightly lower than for dipole g modes, which is possibly because identification of quadrupole modes is more difficult, since the period region overlaps with the harmonics of dipole g modes, and the peaks are generally crowded. This may lead to missing the highest order modes.

Both the dipole and quadrupole g modes are symmetrically distributed. However, the distribution of radial orders of r modes is asymmetric. Most r-modes peaks have the radial order between ∼13 and ∼53 with FWHM of ∼40, which is lower than the g modes.

Fig. 15 summarizes the pattern lengths of the dipole, quadrupole g modes, and r modes, determined as the difference between the largest and smallest radial orders in each star. For the dipole g modes (black histogram), patterns typically span ∼35. Of those, KIC 11571757 has the longest period spacing pattern spanning 73 modes, as shown in the online supplementary material. For the quadrupole g-mode patterns (grey), the typical length is similar to the dipole one. For the r modes (red), the pattern is typically shorter than for g modes. The distribution of r modes shows the excess over that of g modes when the length is smaller than 30. Of those, KIC 5640438 shows the longest r-mode period spacing pattern, which spans 67 radial orders.

To summarize, the distribution of excited radial orders in g modes is symmetric with centre of $n \sim 40$. There are more low-radial-order r modes than g modes, and their distribution is asymmetric. The excited modes generally span tens of radial orders in both g and r modes. Rossby mode patterns show lower radial orders and shorter lengths than the g-mode patterns.

5 CONCLUSIONS

We report 82 γ Dor stars in which the period spacing patterns of both g- and r-modes are seen, which forms the largest sample of γ Dor stars with r modes. The period spacing changes approximately linearly with period due to the near-core rotation but shows some fluctuations caused by chemical composition gradients. In each star, the g and r modes have similar period spacings (around several hundred seconds), but the mean periods of r modes are generally twice those of g modes. We observed some turning points in ΔP for r-modes in several stars, caused by the rapid change of the eigenvalue λ. By fitting a straight line to ΔP versus P, we find that the slope correlates negatively with the mean period in r modes.

The TAR was used to fit the observed patterns and calculate the near-core rotation rates. The fit matched the observed patterns well, and the near-core rotation rate (f_{rot}) and the asymptotic spacing (Π_0) were constrained accurately. Most of the 82 stars have rotation frequencies between 1 and 2 d^{-1}, with Π_0 around 4000 s. We noticed six stars that have surface modulations caused by spots or the ellipsoidal variability in a binary system. Of those, five stars rotate uniformly, whilst KIC 3341457 has a differential core-to-surface rotation. This is consistent with the previous observations that most main-sequence stars rotate quasi-rigidly, whilst components in binary systems are more likely to have non-uniform rotation profile. The radial orders of excited modes display different distributions for the dipole g modes, quadrupole g modes, and r modes. Most g-modes appear around $n \sim 55$, whilst the radial orders of r modes are likely to be between 13 and 50, generally lower than those of g modes.

Our sample is very useful for understanding the physics of rotation and angular momentum transport in main-sequence stars, and can place much needed constraints on diffusive mixing and chemical gradients, whilst also providing stellar ages.

REFERENCES

Aerts C., Molenberghs G., Kenward M. G., Neiner C., 2014, ApJ, 781, 88
Aerts C., Mathis S., Rogers T., 2018a, preprint (arXiv:1809.07779)
Aerts C. et al., 2018b, ApJS, 237, 15
Andersson N., 1998, ApJ, 502, 708
Asplund M., Grevesse N., Sauval A. J., Scott P., 2009, ARA&A, 47, 481
Ballot J., Lignières F., Prat V., Reese D. R., Rieutord M., 2012, in Shibahashi H., Takata M., Lynas-Gray A. E., eds, ASP Conf. Ser. Vol. 462, Progress in Solar/Stellar Physics with Helio- and Asteroseismology. Astron. Soc. Pac., San Francisco, p. 389
Balona L. A., 2017, MNRAS, 467, 1830
Balona L. A., Krisciunas K., Cousins A. W. J., 1994, MNRAS, 270, 905
Bedding T. R., Murphy S. J., Colman I. L., Kurtz D. W., 2015, European Physical Journal Web of Conferences. EDP Sciences - Web of Conferences, France, p. 01005
Benomar O. et al., 2018, Science, 361, 1231
Berthomieu G., Provost J., 1983, A&A, 122, 199
Borucki W. J. et al., 2010, Science, 327, 977
Bouabid M.-P., Montalbán J., Miglio A., Dupret M.-A., Grigahcène A., Noels A., 2011, A&A, 531, A145
Bouabid M.-P., Dupret M.-A., Salmon S., Montalbán J., Miglio A., Noels A., 2013, MNRAS, 429, 2500
Brown E. F., Ushomirsky G., 2000, ApJ, 536, 915
Cazorla C., Nazé Y., Morel T., Georgy C., Godart M., Langer N., 2017, A&A, 604, A123
Christophe S., Ballot J., Ouazzani R.-M., Antoci V., Salmon S. J. A. J., 2018, A&A, 618, A47
Cousins A. W. J., Warren P. R., 1963, Mon. Notes Astron. Soc. South Afr., 22, 65
Couvidat S., García R. A., Turck-Chièze S., Corbard T., Henney C. J., Jiménez-Reyes S., 2003, ApJ, 597, L77
Degroote P. et al., 2011, A&A, 536, A82
Donati J.-F., Landstreet J. D., 2009, ARA&A, 47, 333
Dupret M.-A., Grigahcène A., Garrido R., Gabriel M., Scuflaire R., 2005, A&A, 435, 927
Eckart C., 1960, Hydrodynamics of Oceans and Atmospheres. Pergamon Press, Oxford
Foreman-Mackey D., Hogg D. W., Lang D., Goodman J., 2013, PASP, 125, 306
Gaia Collaboration et al., 2016, A&A, 595, A1
Gaia Collaboration et al., 2018a, A&A, 623, A110
Gaia Collaboration et al., 2018b, A&A, 616, A1
Gaia Collaboration et al., 2018c, A&A, 616, A10
García R. A. et al., 2014, A&A, 572, A34
Guo Z., Gies D. R., Matson R. A., 2017, ApJ, 851, 39
Hatta Y., Sekii T., Takata M., Kurtz D. W., 2019, ApJ, 871, 135
Kallinger T. et al., 2017, A&A, 603, A13
Kaye A. B., Handler G., Krisciunas K., Poretti E., Zerbi F. M., 1999, PASP, 111, 840
Keen M. A., Bedding T. R., Murphy S. J., Schmid V. S., Aerts C., Tkachenko A., Ouazzani R.-M., Kurtz D. W., 2015, MNRAS, 454, 1792
Kirk B. et al., 2016, AJ, 151, 68
Kjeldsen H., 2003, Ap&SS, 284, 1
Koch D. G. et al., 2010, ApJ, 713, L79
Kurtz D. W., Saio H., Takata M., Shibahashi H., Murphy S. J., Sekii T., 2014, MNRAS, 444, 102
Kurtz D. W., Shibahashi H., Murphy S. J., Bedding T. R., Bowman D. M., 2015, MNRAS, 450, 3015
Lee U., Saio H., 1987, MNRAS, 224, 513
Lee U., Saio H., 1997, ApJ, 491, 839
Li G., Bedding T. R., Murphy S. J., Van Reeth T., Antoci V., Ouazzani R.-M., 2019, MNRAS, 482, 1757
Liang Z.-C., Gizon L., Birch A. C., Duvall T. L., Jr, 2018, preprint (arXiv: 1812.07413)
Löptien B., Gizon L., Birch A. C., Schou J., Proxauf B., Duvall T. L., Bogart R. S., Christensen U. R., 2018, Nature Astronomy, 2, 568
Lovelace R. V. E., Romanova M. M., 2014, Fluid Dyn. Res., 46, 041401
Lurie J. C. et al., 2017, AJ, 154, 250
Maeder A., 2009, Physics, Formation and Evolution of Rotating Stars. Springer Berlin Heidelberg, Germany
Mathis S., Zahn J.-P., 2005, A&A, 440, 653
Mathis S., Decressin T., Eggenberger P., Charbonnel C., 2013, A&A, 558, A11
Mathur S. et al., 2017, ApJS, 229, 30
Matijevič G., Prša A., Orosz J. A., Welsh W. F., Bloemen S., Barclay T., 2012, AJ, 143, 123
Mazumdar A. et al., 2014, ApJ, 782, 18
McIntosh S. W., Cramer W. J., Pichardo Marcano M., Leamon R. J., 2017, Nat. Astron., 1, 0086
McQuillan A., Mazeh T., Aigrain S., 2014, ApJS, 211, 24
Miglio A., Montalbán J., Noels A., Eggenberger P., 2008, MNRAS, 386, 1487

Mombarg J. S. G., Van Reeth T., Pedersen M. G., Molenberghs G., Bowman D. M., Johnston C., Tkachenko A., Aerts C., 2019, MNRAS, 485, 3248

Montgomery M. H., Odonoghue D., 1999, Delta Scuti Star Newsletter, 13, 28

Murphy S. J., Fossati L., Bedding T. R., Saio H., Kurtz D. W., Grassitelli L., Wang E. S., 2016, MNRAS, 459, 1201

Murphy S. J., Hey D., Van Reeth T., Bedding T. R., 2019, MNRAS, 485, 2380

Ouazzani R.-M., Salmon S. J. A. J., Antoci V., Bedding T. R., Murphy S. J., Roxburgh I. W., 2017, MNRAS, 465, 2294

Papaloizou J., Pringle J. E., 1978, MNRAS, 182, 423

Pápics P. I. et al., 2017, A&A, 598, A74

Paxton B., Bildsten L., Dotter A., Herwig F., Lesaffre P., Timmes F., 2011, ApJS, 192, 3

Pedlosky J., 1982, Geophysical Fluid Dynamics. Springer-Verlag, Germany

Prat V., Mathis S., Augustson K., Lignières F., Ballot J., Alvan L., Brun A. S., 2018, A&A, 615, A106

Prat V., Mathis S., Buysschaert B., Van Beeck J., Bowman D. M., Aerts C., Neiner C., 2019, preprint (arXiv:1903.05620)

Provost J., Berthomieu G., Rocca A., 1981, A&A, 94, 126

Rossby C. G., 1939, J. Mar. Res., 2, 38

Royer F., Zorec J., Gómez A. E., 2007, A&A, 463, 671

Saio H., 1982, ApJ, 256, 717

Saio H., Kurtz D. W., Takata M., Shibahashi H., Murphy S. J., Sekii T., Bedding T. R., 2015, MNRAS, 447, 3264

Saio H., Kurtz D. W., Murphy S. J., Antoci V. L., Lee U., 2018a, MNRAS, 474, 2774

Saio H., Bedding T. R., Kurtz D. W., Murphy S. J., Antoci V., Shibahashi H., Li G., Takata M., 2018b, MNRAS, 477, 2183

Schmid V. S., Aerts C., 2016, A&A, 592, A116

Screen J. A., Simmonds I., 2014, Nature Climate Change, 4, 704

Shibahashi H., 1979, PASJ, 31, 87

Stumpe M. C., Smith J. C., Catanzarite J. H., Van Cleve J. E., Jenkins J. M., Twicken J. D., Girouard F. R., 2014, PASP, 126, 100

Thompson M. J. et al., 1996, Science, 272, 1300

Townsend R. H. D., 2003, MNRAS, 340, 1020

Townsend R. H. D., 2005, MNRAS, 360, 465

Townsend R. H. D., Teitler S. A., 2013, MNRAS, 435, 3406

Triana S. A., Moravveji E., Pápics P. I., Aerts C., Kawaler S. D., Christensen-Dalsgaard J., 2015, ApJ, 810, 16

Van Reeth T. et al., 2015a, ApJS, 218, 27

Van Reeth T. et al., 2015b, A&A, 574, A17

Van Reeth T. et al., 2018, A&A, 618, A24

Van Reeth T., Tkachenko A., Aerts C., 2016, A&A, 593, A120

Wade G. A., Petit V., Grunhut J. H., Neiner C., MiMeS Collaboration, 2016, in Sigut T. A. A., Jones C. E., eds, ASP Conf. Ser. Vol. 506, Bright Emissaries: Be Stars as Messengers of Star-Disk Physics. Astron. Soc. Pac., San Francisco, p. 207

White T. R., Bedding T. R., Stello D., Christensen-Dalsgaard J., Huber D., Kjeldsen H., 2011, ApJ, 743, 161

Zaqarashvili T. V., Oliver R., Hanslmeier A., Carbonell M., Ballester J. L., Gachechiladze T., Usoskin I. G., 2015, ApJ, 805, L14

Zhang X. B., Fu J. N., Luo C. Q., Ren A. B., Yan Z. Z., 2018, ApJ, 865, 115

SUPPORTING INFORMATION

Supplementary data are available at *MNRAS* online.

Rossby_appendix.pdf

Please note: Oxford University Press is not responsible for the content or functionality of any supporting materials supplied by the authors. Any queries (other than missing material) should be directed to the corresponding author for the article.

APPENDIX A: PERIOD SPACING DIAGRAMS

We show the period spacing patterns, the sideways échelle diagrams, the TAR fit results, and the posterior distributions of 82 γ Dor stars with gravity modes and Rossby modes patterns. Example diagrams are shown in figs A1 to A3. The figures for the other 81 stars are available as supplementary online material.
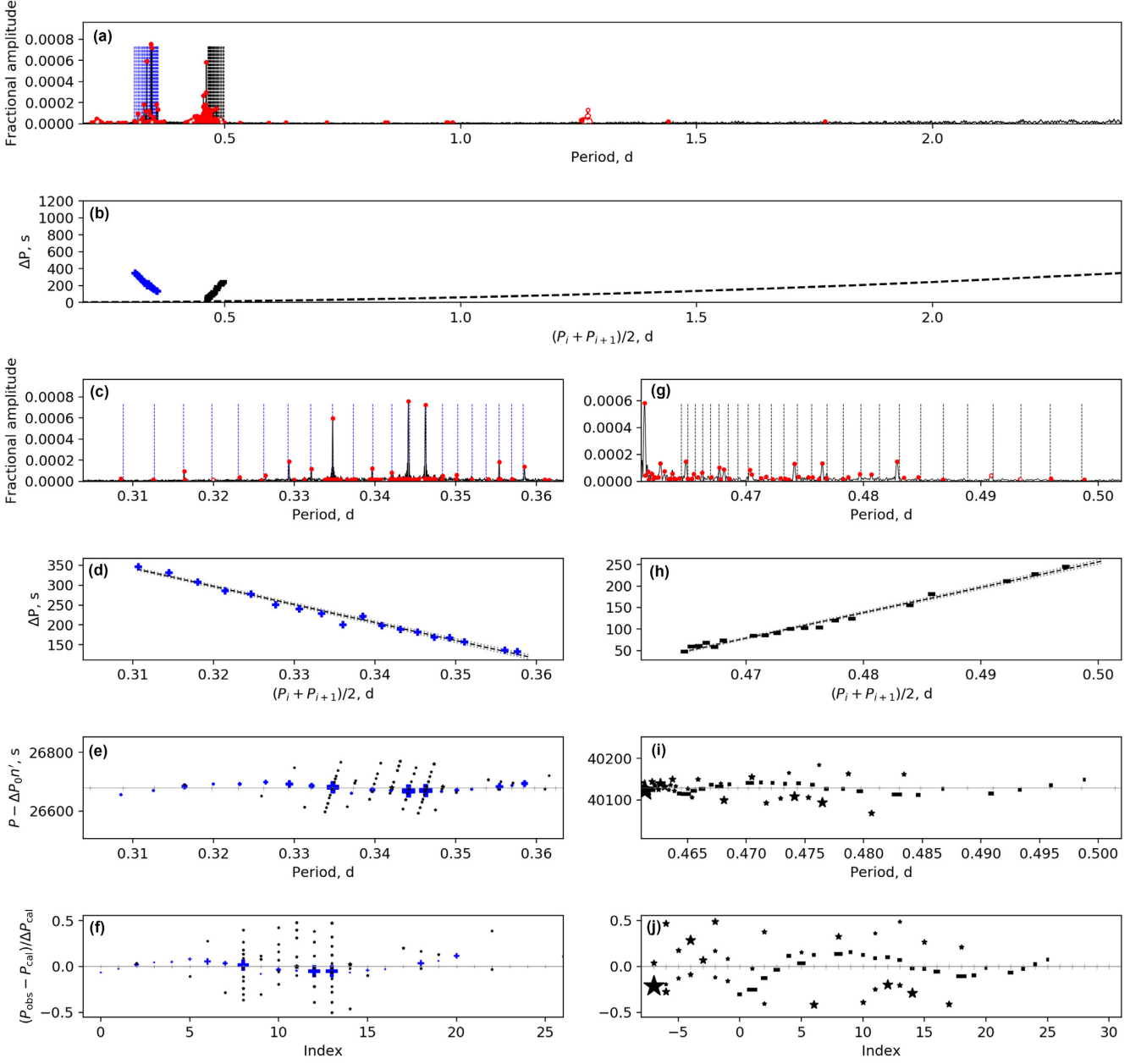
Figure A1. The g and r-mode patterns of KIC 6301745. (a) The amplitude spectrum with *x*-axis of period. The solid red circles present the detected independent frequencies, whilst the open red circles show the combination frequencies. The vertical dashed lines are the linear fits for each pattern. The *x*-axis range is set from 0.2 to 2.4 d for consistency for all stars. There are two period spacing patterns. The blue one on the left is the $l = 1$, $m = 1$ g modes, whilst the black one on the right is the $k = -2$, $m = -1$ r modes. (b) The period spacing patterns of KIC 6301745. The linear fits and uncertainties are shown by the black and grey dashed lines. The blue plus symbols are the g modes and the black minus symbols are the r modes. The dashed line is the period resolution. (c) and (d) The detail of the spectrum and period spacing pattern of g modes. (e) The sideways échelle diagram of the g pattern. The black stars are the messy peaks. (f) The normalized sideways échelle diagram of the g-modes pattern. (g) to (j) Same but for the r-mode pattern.
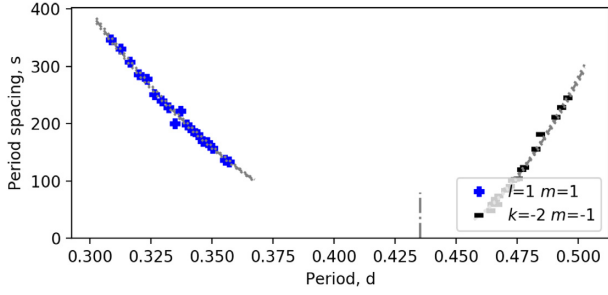
Figure A2. The TAR fit of KIC 6301745. The blue plus symbols show the $l = 1$, $m = 1$ gravity modes and the black minus symbols show the $k = -2$, $m = -1$ Rossby modes. The dashed grey curves display the best-fitting result. The error margins are plotted by the dotted lines. The vertical dashed line denotes the fitted rotation period.
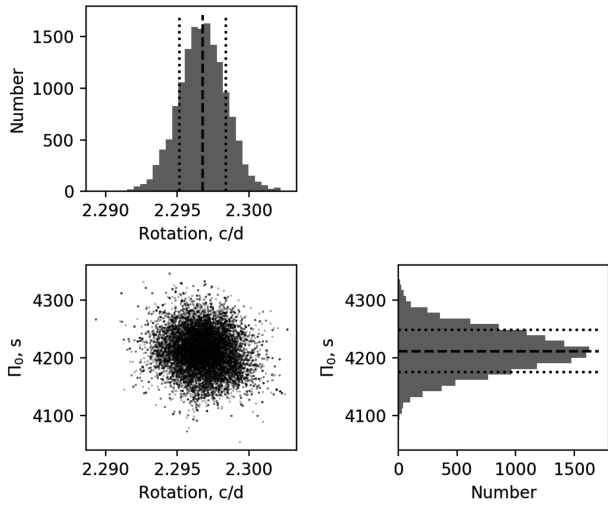

Figure A3. The posterior distributions for the TAR fit to KIC 6301745 using equation (9). The dashed lines are the medians and the dotted lines show the $\pm 1\sigma$ areas.

## APPENDIX B: SURFACE MODULATIONS

We present six stars with surface modulations in this appendix. KIC 3341457 displays a strong radial differential rotation, whilst the other five stars show uniform rotation (see Figs B1–B6).
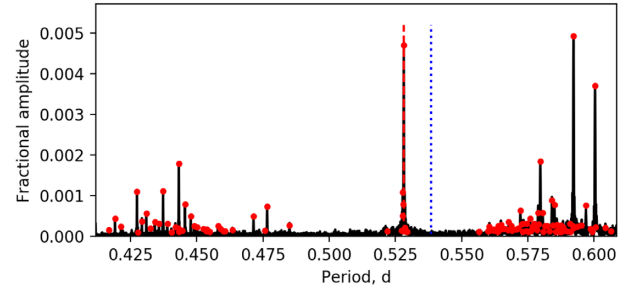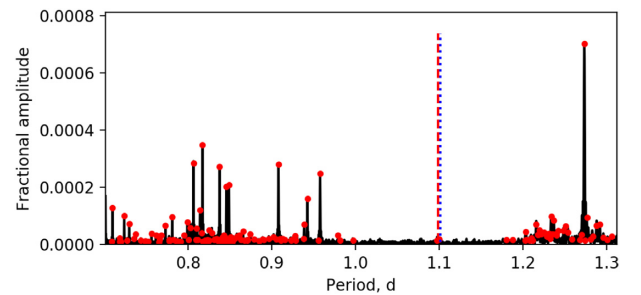

Figure B1. The periodogram and surface rotation of KIC 3341457. The red dots are peaks with S/N > 4. The peak groups at 0.528 d is the signal of the surface modulation. The blue dotted line displays the near-core rotation, whilst the red dashed line shows the surface rotation, which is the mean of the peaks.
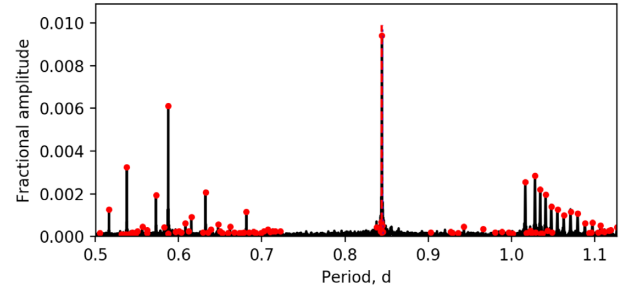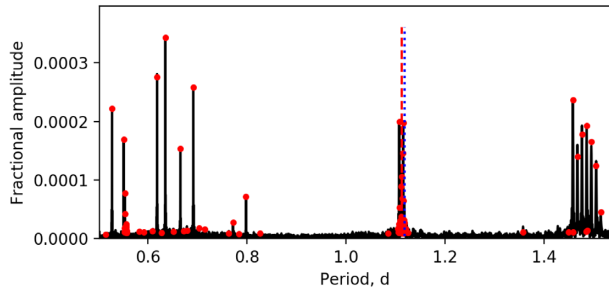

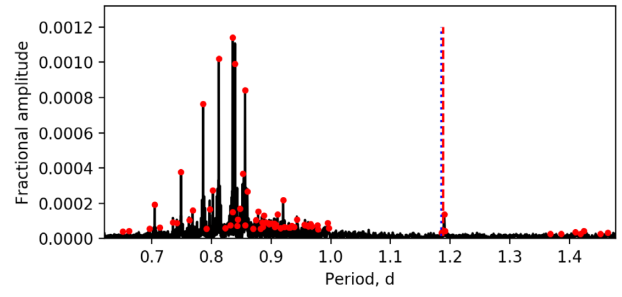**Figure B2.** The periodogram and surface rotation of KIC 7596250.
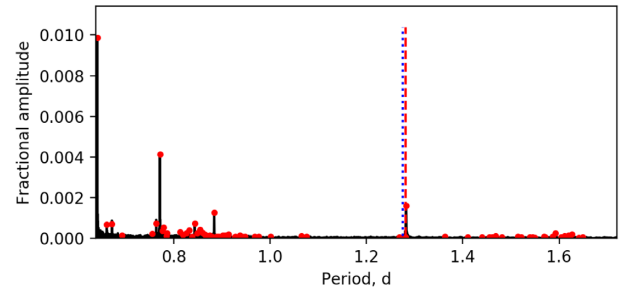
Figure B3. The periodogram and surface rotation of KIC 7621649.

Figure B4. The periodogram and surface rotation of KIC 9652302.

Figure B5. The periodogram and surface rotation of KIC 9716563.

Figure B6. The periodogram and surface rotation of KIC 10423501.

This paper has been typeset from a TEX/LATEX file prepared by the author.